





Environmental effects as a key factor in shaping star-forming S0 galaxies

Pei-Bin Chen (陈培彬)¹, Jun-Feng Wang (王俊峰)^{1,*}, Yan-Mei Chen (陈燕梅)², Xiao-Yu Xu (许啸宇)^{3,4},
Tian-Wen Cao (曹天文)¹

¹ Department of Astronomy, Xiamen University, Xiamen, Fujian 361005, China

² Department of Astronomy, Nanjing University, Nanjing 210093, China

³ School of Astronomy and Space Science, Nanjing University, Nanjing 210023, China

⁴ Key Laboratory of Modern Astronomy and Astrophysics, Nanjing University, Nanjing 210023, China

Accepted XXX. Received YYY; in original form ZZZ

ABSTRACT

Context. The origins of lenticular galaxies (S0s) can be classified into two main categories: “minor mergers” in low-density environments (LDEs) and “faded spirals” in high-density environments (HDEs). The transitional phase in the evolution of S0s, namely, star-forming lenticular galaxies (SFS0s), can serve as an important probe for analyzing the complex processes involved in the transformation between different galaxy types and the quenching of star formation (SF).

Aims. We attempt to find the impact of different environments on the global properties and spatially resolved quantities of SFS0s.

Methods. We selected 71 SFS0s from the SDSS-IV MaNGA Survey, comprising 23 SFS0s in HDEs (SFS0s_HE) and 48 SFS0s in LDEs (SFS0s_LE). We examined the effects of the environment, by studying the global properties, concentration index, and radial profiles of the derived quantities.

Results. The varied environments of SFS0s do not lead to any significant difference in global properties (e.g., Sérsic index). By calculating $CI_{H\alpha/\text{cont}}$, we observe that different environments may cause varying concentrations of SF. Specifically, SFS0s_LE, affected by external gas mergers or inflow, exhibit a more centrally concentrated SF (i.e., larger $CI_{H\alpha/\text{cont}}$). This trend is further supported by $CI_{\text{SFR},H\alpha}$, which only considers the gas disk of the galaxy. This observation is aligned with the observed shrinking of gas disks in galaxies affected by ram-pressure stripping in HDEs. Furthermore, their Σ_{SFR} or resolved sSFR are comparable. On average, SFS0s_LE display significantly higher values for both quantities. Finally, the observed D_n4000 and gas-phase metallicity gradient correspond well to their assumed origins. However, we did not find a significantly lower gas-phase metallicity in SFS0s_LE.

Conclusions. We suggest that different environments (i.e., origins) do not have a significant impact on the global properties of SFS0s, but they do indeed affect the distribution of SF. Considering the size of our sample and the unique nature of the galaxy, additional atomic and molecular gas data may provide further details to improve our understanding of these systems.

Key words. Lenticular galaxies - Galaxy evolution - Galaxy environment

1. Introduction

Substantial efforts have been devoted to understanding the correlation between galaxies and their environments (e.g., Vollmer 2013; Kolcu et al. 2022; Pérez-Millán et al. 2023). Numerous studies have shown that the environments of galaxies affect their color, gas content (e.g., Boselli & Gavazzi 2006), and galaxy interactions, which then affect their morphology (e.g., Dressler 1980), current star formation (SF; e.g., Lewis et al. 2002; Vollmer 2013), and SF history (SFH; e.g., Aird et al. 2012). Galaxies can be broadly classified based on morphology into elliptical galaxies (EGs), spiral galaxies (SGs), and the intermediate form known as lenticular galaxies (S0s; Hubble 1936). In general, EGs and S0s are referred to as early-type galaxies (ETGs; e.g., Chen et al. 2023), while SGs are referred to as late-type galaxies (LTGs). Observations show that quenched galaxies tend to have early-type morphology (e.g., Bait et al. 2017). This is not surprising, as ETGs are typically massive galaxies in high-density environments (HDEs; Dressler 1980). The concept that ETGs are passive and red death systems is widely accepted (e.g., Strateva et al. 2001; Xu et al. 2022). However, recent obser-

vations indicate that some ETGs contain atomic gas, even dust and/or molecular gas. Their star formation (SF) activities have been revealed through far-ultraviolet (FUV) and infrared (IR) radiation (Davis et al. 2014) or emission-line diagnostic analysis (e.g., Xiao et al. 2016; Chen et al. 2023).

Many works are dedicated to studying the origin of blue ETGs. Schawinski et al. (2009) found a sample of 204 blue ETGs exhibiting mild to moderate star formation rates (SFRs) between $0.05 \sim 50 M_{\odot}\text{yr}^{-1}$. They discussed the possible positions that blue ETGs may occupy in the overall evolutionary picture. Moreover, they found that their gas-phase metallicity is all supersolar, which is consistent with the mass-metallicity relation (Tremonti et al. 2004). Kannappan et al. (2009) identified a population of morphologically defined EGs/S0s lying on the locus of LTGs in the color-stellar mass (M_*) space (the blue sequence) at the present epoch. They studied the proportions of these galaxies at three mass scales (i.e., shutdown mass, bimodality mass, and threshold mass) of interest. Moreover, Oser et al. (2010) used large-scale dark matter simulation to recover the observational result of “archaeological downsizing,” indicating that ETGs have a two-phase formation process: in situ SF and external accretion. Of course, earlier studies have also provided

* E-mail: jfwang@xmu.edu.cn

empirical evidence prior to this (e.g., Aragon-Salamanca et al. 1998; Laine et al. 2004) and a large amount of observational evidence has been obtained to support this claim (e.g., Donzelli et al. 2011; Forbes et al. 2011; Cappellari et al. 2013). Specifically, Cappellari et al. (2013) used the volume-limited and nearly mass-selected ATLAS^{3D} sample of 260 ETGs to study their distributions in the mass-size and mass- σ planes. They also discovered the three characteristic mass scales and found evidence of this “two-phase” character (see their Figs. 15 and 16). As one of the components of ETGs, S0s have attracted much attention (e.g., Gunn & Gott 1972; Dressler et al. 2004; Boselli et al. 2006; Querejeta et al. 2015; Coccato et al. 2022).

Generally, S0s exhibit a central bulge surrounded by a disk but lack prominent spiral arms. Interestingly, Bait et al. (2017) found that S0s are quite abundant in various environments (see their Fig. 12) and their specific SFR (sSFR) spans several orders of magnitude (see their Fig. 6), from the red sequence (red sequence galaxies, RSGs) to the green valley (green valley galaxies, GVGs) to the blue cloud (star-forming galaxies, SFGs). Numerous studies have revealed significant differences in the characteristics of S0s (photometric, spectroscopic, and kinematic; e.g., Barway et al. 2013) in different environments and cover a certain range (Fraser-McKelvie et al. 2018), suggesting multiple and complex formation pathways. So far, the formation pathways of S0s can be divided into two major categories (faded spiral and minor merger). The variation in the fraction of S0s in different environments is exactly the opposite of the variation in SGs (Dressler 1980; Dressler et al. 1997; Bait et al. 2017). Thus, considering the similar structure and kinematic characteristics ($V_{\text{rot}}/\sigma > 1$; Coccato et al. 2020; Deeley et al. 2020, 2021) between the two types, it is generally believed that S0s originate from the fading of SGs. Investigations into S0s across diverse environments have unveiled that those with significant gaseous emission are primarily located in the field and on the outskirts of galaxy clusters, suggesting that the gas either undergoes stripping when galaxies fall into galaxy clusters or the increased gas content results from the infall or merger of external fresh gas (e.g., Deeley et al. 2021). This hypothesis finds support in various studies (e.g., Gunn & Gott 1972; Barway et al. 2009; Kormendy & Bender 2012; Mishra et al. 2018; Coccato et al. 2020; Deeley et al. 2020, 2021; Boselli et al. 2022), suggesting that it is more prevalent in HDEs such as galaxy groups and clusters, often referred to as “faded spirals,” where SGs lose their gas and SF is rapidly quenched.

However, this pathway does not explain the apparent difference between the observed features of the S0s and the expected properties of ancestral SGs. Investigations into S0s in low-density environments (LDEs, fields) have unveiled distinct properties (e.g., Diaz et al. 2018; Coccato et al. 2022; Deeley et al. 2020). For instance, S0s in LDEs exhibit redder bulges in comparison to their disks (Tabor et al. 2017). Coccato et al. (2020) compared the spatially resolved kinematics of 21 S0s from an extreme environment with the overall stellar populations (SPs) and found that S0s in the field exhibited more pressure-supported ($V_{\text{rot}}/\sigma < 1$), which indicates that mergers or gas accretions (minor merger; Cappellari et al. 2013; Cappellari 2016) shape their kinematic characteristics. Deeley et al. (2020) studied 219 S0s from the SAMI Survey and found that minor mergers dominated in isolated galaxies and small groups. Similarly, Coccato et al. (2022) carried out a study on 329 S0s from the SAMI and MaNGA surveys and showed that the minor merger is a viable channel. Furthermore, the presence of decoupled gas kinematics in isolated S0s also supports external sources of gas (Katz et al. 2014). In addition, simulations have also sup-

ported this channel (e.g., Querejeta et al. 2015; Eliche-Moral et al. 2018; Deeley et al. 2021). This type of channel is popular in LDEs (e.g., Deeley et al. 2021; Coccato et al. 2022), such as fields.

Today, studying S0s that are still undergoing SF activity is very interesting. A transitional phase in the evolution of S0s, star-forming lenticular galaxies (SFS0s), serve as important probes for understanding the complex processes involved in the transformation between different galaxy types and the quenching of star formation. Xiao et al. (2016) studied 583 S0s from SDSS Data Release 7 (DR7) and found that only 8% of them showed central SF activity; these active S0s have lower stellar mass (M_*) and are more inclined to sparse environments. Xu et al. (2022) studied 52 star-forming S0s (SFS0s) from the SDSS-IV MaNGA Survey and found the presence of pseudo bulges and different dynamic processes in SFS0s. Moreover, they found that the number of SFS0s in the LDEs is twice that in the HDEs, even though the normal S0s favored the HDEs (Dressler et al. 1997). Similarly, Rathore et al. (2022) used sSFR (Salim 2014) as a criterion to study 120 SFS0s from the SDSS-IV MaNGA Survey and found that the SF of these galaxies is center-dominated rather than disk-dominated. These previous works all suggest that SFS0s also have two main formation pathways, as mentioned above. In this work, we accept these two formation pathways in different environments, studying the environmental effects on the global and derivative properties of SFS0s.

We utilized integral field spectroscopy (IFS) data obtained from the Mapping Nearby Galaxies of the Sloan Digital Sky Survey at APO (SDSS-IV MaNGA, Bundy et al. 2015; Law et al. 2015; Blanton et al. 2017). The MaNGA data allow for the analysis of spatially resolved dynamics and chemical compositions in galaxies, providing crucial information about their formation and evolution. Utilizing 17 simultaneous integrated field units (IFUs), each comprising a closely packed array of optical fibers, MaNGA conducted spectroscopic measurements across the surfaces of approximately 10,000 nearby galaxies (Bundy et al. 2015; Law et al. 2015; Blanton et al. 2017). This approach generates 2D maps representing various physical quantities such as stellar and ionized gas velocities, facilitating a comprehensive understanding of the “life history” of galaxies. These maps provide insights into the birth, assembly, ongoing growth through SF and merger processes, and eventual quenching at later stages (e.g., Bundy et al. 2015). The observed spectrum covers a wavelength range from 3600 Å to 10300 Å, with a spectral resolution of approximately 2000. Notably, the observations span at least 1.5 effective radii (R_e) for the target galaxy, where R_e denotes the radius containing 50% of the galaxy’s light.

In this work, we constructed a sample of 71 SFS0s in various environments from the SDSS-IV MaNGA survey. Our purposes are: 1) To find out whether SFS0s have different global properties (e.g., Sérsic index) in different environments; 2) We attempted to establish the relationship between the derivation quantities (e.g., concentration index, D_n4000 , metallicity) of SFS0s and its different formation pathways. This paper is organized as follows: Our sample selection is presented in Sect. 2, as well as the environmental information of galaxies. We provide the methodology in Sect. 3, including extinction correction, the description of morphological parameters, and how to construct radial profiles of derivation quantities. Section 4 provides our results and the related discussion listed in Sect. 5. Finally, we list our summary in Sect. 6. Throughout this paper, we adopt a set of cosmological parameters as follows: $H_0 = 70 \text{ km s}^{-1} \text{ Mpc}^{-1}$ (i.e., $h = 0.7$), $\Omega_m = 0.30$, and $\Omega_\Lambda = 0.70$.

2. Data and sample selection

2.1. Data

We utilized the data products from MaNGA (Bundy et al. 2015; Yan et al. 2016) DR 17 (Abdurro'uf et al. 2022). The primary data products from MaNGA encompass 3D calibration data cubes generated through the Data Reduction Pipeline (DRP) and 2D maps of derived quantities produced by the Data Analysis Pipeline (DAP) using these cubes. The DAP constructs 2D maps of the derived quantities, including information on stellar, gas, and emission lines, by analyzing individual or binned groups of pixels. The final data cubes provide spectra for each pixel of a target, with each pixel covering an area of $0.''5 \times 0.''5$. In this work, we utilized the DAP 2D maps (“HYB10-MILESHC-MASTARSSP”¹) of the derived quantities. Additionally, MaNGA targets have undergone processing with the Pipe3D IFS data-processing pipeline (Sánchez et al. 2016b,a). We extracted spatially resolved stellar mass (M_*) and stellar mass surface density (Σ_*) from Pipe3D data cubes². Other intrinsic properties, including redshift, axis ratio (b/a), and R_e , were sourced from NASA-Sloan Atlas (NSA) catalog³ (v1_0_1, Blanton et al. 2011). Morphological (Domínguez Sánchez et al. 2022; Vázquez-Mata et al. 2022), environmental (Argudo-Fernández et al. 2015; Etherington & Thomas 2015; Wang et al. 2016) and photometrical (Domínguez Sánchez et al. 2022) information was sourced from the MaNGA value-added catalogs (MaNGA_VAC⁴).

2.2. Sample selection

MaNGA_VAC provides a Deep Learning Catalogue (hereafter MDLM_VAC) based on the morphological classification of the final MaNGA DR17 galaxy sample (Domínguez Sánchez et al. 2022). The methods for training and testing the Deep Learning model were described in detail in Domínguez Sánchez et al. (2022). These methods are based on a previous work (Domínguez Sánchez et al. 2018), which provided the classification for about 670,000 objects from SDSS DR7 Main Galaxy Samples. Furthermore, following the method provided by Vázquez-Mata et al. (2022), MaNGA_VAC provides a pure visual morphology classification catalog (hereafter, MaNGA_visual_morpho), covering all galaxies in MaNGA DR17. This classification is derived from the inspection of image mosaics, utilizing a new re-processing of SDSS and Dark Energy Legacy Survey (DESI) images. The classification includes 13 Hubble types and notes the presence of bars and bright tidal debris. Therefore, our selection comprises the following:

- We selected galaxies that pass the basic selection criteria and have “ $T_Type \leq 0$ ”, “ $P_LTG < 0.5$ ”, “ $P_S0 > 0.5$ ” and “ $VC = 2$ ” as recommended by MDLM_VAC for identifying S0s. To create a sample containing only S0s, we cross-reference with MaNGA_visual_morpho to ensure that the “Hubble-type” of the galaxy is S0. Moreover, we excluded the unreliable classification sources (Unsure = 1). Finally, we cross-referenced with the Pipe3D catalog (Sánchez

2020) and the photometric catalog (Domínguez Sánchez et al. 2022) to obtain a parent sample.

- Once the parent sample is established, understanding the environmental information of the galaxy becomes crucial. A common method is to measure the projected density to the N th nearest group galaxy (e.g., Ellison et al. 2018). Information on the local environment of galaxies is provided in the MaNGA_VAC GEMA catalog (hereafter, GEMA_VAC; Argudo-Fernández et al. 2015), where the projected number density parameter ($\eta_{k,LSS}$, i.e., eta_k) of the galaxy is defined as:

$$\eta_{k,LSS} = \log\left(\frac{k-1}{\text{Vol}(d_k)}\right) = \log\left(\frac{3(k-1)}{4\pi d_k^3}\right) \quad (1)$$

where d_k is the projected physical distance to the k th nearest neighbour, with k is equal to 5 (Balogh et al. 2004; Xiao et al. 2016; Johnston et al. 2022).

- By cross-matching the above parent sample with GEMA_VAC, we obtained a sample containing environmental information (hereafter Sample_A). According to the definition of “eta_k” (formula 1), Sample_A is divided into two samples: S0s with an eta_k value in HDEs (e.g., galaxy clusters and groups, hereafter Sample_HE) and S0s without an eta_k value in LDEs (e.g., fields, hereafter Sample_LE). Importantly, for Sample_LE, even if they are located in LDEs, some galaxies may make up pairs. Previous works have highlighted the fact that environmental influences on galaxy properties extend beyond cluster cores, affecting all groups with a projection density exceeding $1 \text{ galaxy } Mpc^{-2}$ (Lewis et al. 2002). Here, we exclude paired galaxies to obtain a pure LDEs sample (hereafter, Sample_LENp).
- We further require that the axis ratio (b/a) is greater than 0.32 (see Sect. 3.2) to avoid the edge-on situation (e.g., Xu et al. 2022). Finally, we employed the emission line flux (H_α $\lambda 6563$, H_β $\lambda 4861$, [O III] $\lambda 5007$ and [N II] $\lambda 6583$) fitted within $1 R_e$ (signal-to-noise ratio, S/N of ≥ 3) provided by the Pipe3D catalog (Sánchez 2020) to perform a global Baldwin, Phillips & Telervich (BPT, Baldwin et al. 1981) diagnosis of our two samples (i.e., Sample_HE and Sample_LENp). This diagnosis helped us to select galaxies located in the H II regions (Fig. 1). Although active galactic nucleus-host (AGN-host) S0s are excluded in our work, the proportion of AGN-host S0s present in our two parent samples (Sample_HE and Sample_LENp) is close (8% and 11%), so the bias caused by such screening does not depend on the galaxy’s environments, even though different environments have different perturbation mechanisms (Boselli et al. 2022; Cattorini et al. 2023). The slightly higher proportion of AGN-host S0s in LDEs is consistent with previous works (Xiao et al. 2016). Furthermore, it is required that these galaxies have an H_α equivalent width $> 6 \text{ \AA}$ within the center of $2.5''$ to ensure that the final targets are SFGs (Sánchez 2020; Xu et al. 2022).

Following these screening steps, we obtained two parent samples: Sample_HE and Sample_LENp. Then, through the fourth step detailed above, we obtained the final samples for our study: 23 (SFS0s_HE) and 48 (SFS0s_LE). The number of SFS0s in LDEs is about twice that in HDEs, which is consistent with previous results (Xiao et al. 2016; Xu et al. 2022). The basic information for both samples is listed in Table 1, and the detailed information of our targets is listed in Tables A.1 and A.2.

¹ https://data.sdss.org/sas/dr17/manga/spectro/analysis/v3_1_1/3.1.0/HYB10-MILESHC-MASTARSSP/

² https://data.sdss.org/sas/dr17/manga/spectro/pipe3d/v3_1_1/3.1.1/

³ https://data.sdss.org/datamodel/files/ATLAS_DATA/ATLAS_MAJOR_VERSION/nsa.html

⁴ https://www.sdss.org/dr17/data_access/value-added-catalogs/

It is worth emphasizing that the final sample (SFS0s) obtained is only a very small part of the S0 population and may not represent all local S0s (e.g., [Boselli et al. 2022](#)). In addition, we selected galaxies from a deep-learning catalog based on morphological classification, so there is a certain probability of contamination from SGs. We visually examined the deeper DESI images and found that such contamination was very small (about 8%). Subsequent comparisons have indicated that this is not expected to significantly affect our results (see Sect. 4.3).

3. Methodology

3.1. Extinction correction

To calculate the derived quantities of each pixel related to SF (e.g., SFR), we take into account dust extinction, a factor considered in many studies (e.g., [Bao et al. 2021](#); [Xu et al. 2022](#)). [Calzetti \(2001\)](#) estimated the extinction-corrected H_α luminosity using the H_α/H_β ratio:

$$f_i(\lambda) = f_o(\lambda) \times 10^{0.4E(B-V)_{\text{gas}}\kappa^e(\lambda)} \quad (2)$$

where $f_i(\lambda)$ is the intrinsic flux density, $f_o(\lambda)$ is the observed flux density, the color excess $E(B - V)$ is:

$$E(B - V) = 2.15 \times \log[(L_{H_\alpha}/L_{H_\beta})/(L_{H_\alpha}/L_{H_\beta})_i] \quad (3)$$

Here, L_{H_α}/L_{H_β} is the observed ratio, $(L_{H_\alpha}/L_{H_\beta})_i = 2.86$ is an intrinsic Balmer decrement corresponding to Case B recombination with a temperature of 10^4 K and electron density $n_e = 10^2 \text{ cm}^{-3}$ ([Calzetti 2001](#)). Furthermore, $\kappa^e(\lambda)$ is the Galactic dust attenuation curve, expressed as ([Calzetti 2001](#)):

$$\kappa^e(\lambda) = 1.17 \times (-1.857 + 1.040/\lambda) + 1.78 \quad \text{for } 0.63 \mu\text{m} \leq \lambda \leq 2.20 \mu\text{m} \quad (4)$$

and:

$$\kappa^e(\lambda) = 1.17 \times (-2.156 + 1.509/\lambda - 0.198/\lambda^2 + 0.011/\lambda^3) + 1.78 \quad \text{for } 0.12 \mu\text{m} \leq \lambda < 0.63 \mu\text{m} \quad (5)$$

Therefore, the SFR of each pixel is estimated from the extinction-corrected H_α luminosity as presented by [Kennicutt \(1998\)](#) with the Salpeter initial mass function (IMF, [Salpeter 1955](#)):

$$\text{SFR}(M_\odot \text{yr}^{-1}) = 7.9 \times 10^{-42} L_{H_\alpha} \quad (6)$$

The mixing between gas and dust assumed in the extinction law of [Calzetti \(2001\)](#) may not apply to the nearby S0s, as it has been found that the emission gas of some S0s is mainly located on their disk structures ([Boselli et al. 2022](#)). Using this method to correct the observational data may overestimate star formation in the galaxy center regions, but this overestimation does not depend on the environment. In this paper, when calculating the quantities related to SF (e.g., SFR), we performed spatially resolved BPT diagnosis (similar to [Figure 1](#)) for each galaxy, concentrating on the star-forming pixels. Similarly, we also require that the S/N of the emission lines (H_α $\lambda 6563$, H_β $\lambda 4861$, $[\text{O II}] \lambda 3726, 3729$, $[\text{O III}] \lambda 4959, 5007$, and $[\text{N II}] \lambda 6583$) ≥ 3 .

3.2. Radial profiles

Quantities such as SFR surface density (Σ_{SFR}) and resolved sSFR (rsSFR) are crucial for studying galaxy evolution at spatially resolved scales using IFS data (e.g., [Ellison et al. 2018](#); [Bluck et al. 2020](#)). Analyzing physical quantities in galaxies through radial profiles, which represent the azimuthally averaged quantities as a function of distance from the galaxy's center, is a convenient approach. To compute these radial profiles, we utilize the Astropy-affiliated package Photutils: "photutils.aperture" ([Bradley et al. 2022](#)). The construction of our radial profiles is detailed as follows:

- We specify the surface brightness peak of the galaxy as the center for constructing the aperture. To ensure alignment with the galaxy's center and major axis, we visually inspected the deeper DESI images of each galaxy. Briefly, elliptical apertures were created on the maps of Σ_{SFR} , rsSFR, $D_n 4000$, and gas-phase metallicity. The ellipticity (ε) and position angle of each galaxy determine the parameters for constructing these apertures. Subsequently, we obtain the rsSFR map by taking the ratio of Σ_{SFR} and Σ_* maps pixel-by-pixel.
- The semi-major axis of the central elliptical aperture was established at $0.2R_e$, followed by the creation of successive annuli with a thickness of $0.2R_e$ ($0.2R_e$ bin) along the major axis of the galaxy. This process continued until the semi-major axis of the outermost ellipse reaches the boundary of the galaxy's IFU field of view. [Figure 2](#) is an example of our construction on the Σ_* map of one of the galaxies.
- Lastly, the median value represents the corresponding radial bins. For each galaxy, we utilized the observational error⁵ of H_α and the error of Σ_* to compute the error of Σ_{SFR} /rsSFR within a radial bin. Similarly, the observed errors of the emission lines ($[\text{N II}] \lambda 6583$; $[\text{O II}] \lambda \lambda 3726, 3729$; $[\text{O III}] \lambda \lambda 4959, 5007$) and the continuous spectrum in the DAP map files were used to calculate the corresponding errors for gas-phase metallicity and $D_n 4000$, respectively.

Galaxies have a certain inclination angle, impacting surface density-related quantities (e.g., [Wang et al. 2019](#)). To correct the projection effect, a simple trigonometric correction involves multiplying by the scale factor "sec(i)", where "i" is the inclination angle of the galaxy. The "i" is defined as ([Rathore et al. 2022](#)):

$$\cos^2 i = \begin{cases} \frac{(1-\varepsilon)^2 - (1-\varepsilon_{\text{max}})^2}{1 - (1-\varepsilon_{\text{max}})^2}, & \text{if } \varepsilon < \varepsilon_{\text{max}} \\ 0, & \text{if } \varepsilon > \varepsilon_{\text{max}} \end{cases} \quad (7)$$

where ε_{max} is the approximate ellipticity exhibited by an edge-on SG, set at 0.8. The underlying assumption is that the outermost isophote of disk galaxies is approximately circular, with the inclination angle affecting only lengths perpendicular to the major axis. To ensure the validity of de-projection formulation (formula 7), it is crucial that the inclination angle of the galaxy is below 75° ([Rathore et al. 2022](#)). By applying the definition of the "i" (formula 7) and ε ⁶, we identify the selected targets meeting the criterion, where the b/a of a galaxy is greater than 0.32.

⁵ In the MaNGA DAP map file, the inverse variance (Ivar) corresponding to each emission line is provided, which is equal to the reciprocal of the square of the corresponding physical quantity error, i.e., $\text{Error} = 1/\sqrt{\text{Ivar}}$

⁶ If the inclination angle of a galaxy is less than 75° , the corresponding ellipticity is less than 0.68. According to the relationship between the ellipticity and axis ratio: $\varepsilon = 1 - b/a$, we require the axis ratio to be greater than 0.32 in [Section 2.1](#).

Table 1: Basic information of our samples

Samples (1)	Size (2)	$\log(M_*/M_\odot) \geq 10.25$ (3)	$\log(M_*/M_\odot) < 10.25$ (4)	Sérsic index ≥ 2 (5)	Sérsic index < 2 (6)
SFS0s_HE	23	9 (39.1%)	14 (60.9%)	10 (43.5%)	13 (56.5%)
SFS0s_LE	48	15 (31.3%)	33 (68.2%)	13 (27.1%)	35 (72.9%)

Notes: In this table, $\log(M_*/M_\odot) = 10.25$ is the division of stellar mass from Rathore et al. (2022) and Sérsic index of bulges come from the MaNGA-VAC photometry catalog. The percentage in parentheses represents the corresponding proportion of the galaxy.

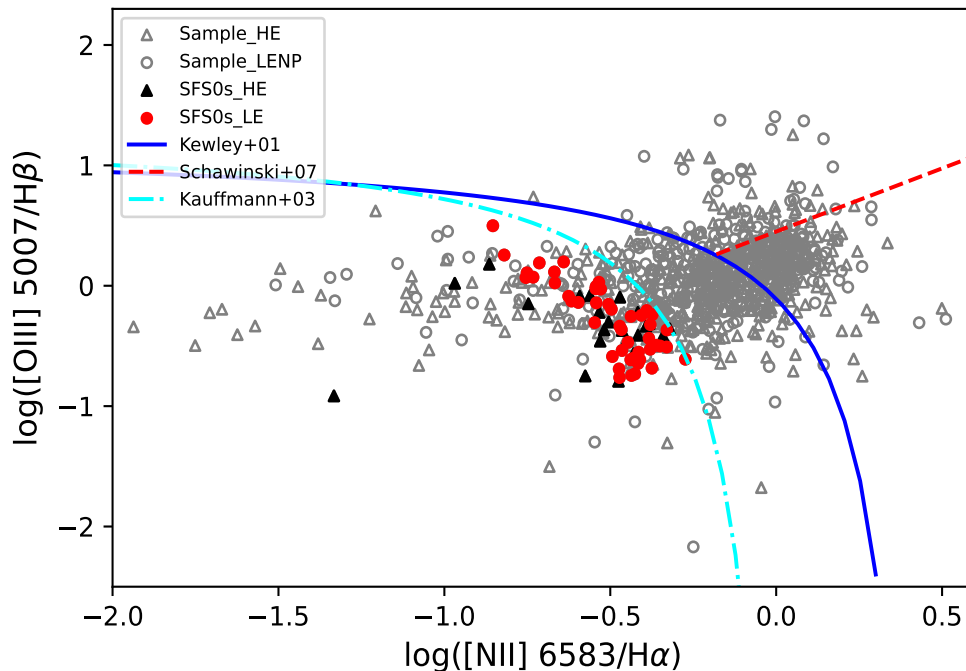


Fig. 1: Global BPT diagnosis of our samples. The cyan dotted line, blue solid line, and red dashed line are the theoretical curves from Kauffmann et al. (2003), Kewley et al. (2001), and Schawinski et al. (2007), respectively. The marks of a triangle in this figure are Sample_HE, while the marks of a circle represent Sample_LEN. Our SFS0s_HE galaxies are represented by the black-filled triangles, and the red-filled circles represent sample SFS0s_LE. Y-axis is the $\log([\text{OIII}] 5007/\text{H}\beta)$, and X-axis is the $\log([\text{NII}] 6583/\text{H}\alpha)$, both from Pipe3D v3_1_1 catalog.

3.3. Gas-phase metallicity

The gas-phase metallicity serves as a crucial diagnostic tool as it tracks the immediate enrichment history of the interstellar medium (ISM) due to the stellar evolution and metal production across the galaxy. Since stellar evolution operates on longer timescales, short-term fluctuations in the gas outflow and inflow significantly impact the observed metallicity distributions. Therefore, studying gas-phase metallicity becomes a key approach to unraveling the origin and motions of gas on galactic scales (Smirnova-Pinchukova et al. 2022). The two primary formation pathways of “faded spiral” and “minor merger” are intricately linked to the interaction types between the galaxy and its environments (e.g., Vollmer 2013; Hwang et al. 2019; Boselli et al. 2022). A significant distinction between these two approaches lies in whether the galaxy acquires new gas (“minor merger”) or loses its original gas (“faded spiral”). Shields et al. (1991) showed that some SGs located in the Virgo cluster exhibit an increase in the metallicity of nearly 0.2 dex, while galaxies located on the outskirts of the Virgo cluster have similar abundances, compared to their counterparts in sparse environments.

Of course, Boselli & Gavazzi (2006) used a larger sample to show that gas-poor LTGs in nearby clusters are more metal-rich than field galaxies. All these studies suggest that gas content may affect the chemical abundance of galaxies and that H I deficiency often occurs when galaxies are forced to lose gas due to environmental effects, which may indicate that the environment of the galaxy played a role in the chemical evolution of the galaxy (e.g., Shields et al. 1991; Boselli & Gavazzi 2006; Hughes et al. 2013). Considering the fact that the external fresh gas (circumgalactic medium, CGM; intergalactic medium, IGM; companions or satellite; Kewley & Dopita 2002; Hwang et al. 2019) is mainly at a low metallicity (Hwang et al. 2019; Smirnova-Pinchukova et al. 2022), the gas-phase metallicity gradient in a system with external fresh gas merging or inflow should be either flat or diluted (e.g., Ellison et al. 2008; Kewley et al. 2010). Therefore, we attempted to investigate the differences in the gas-phase metallicity of SFSOs in different environments, as described in Sect.

4.

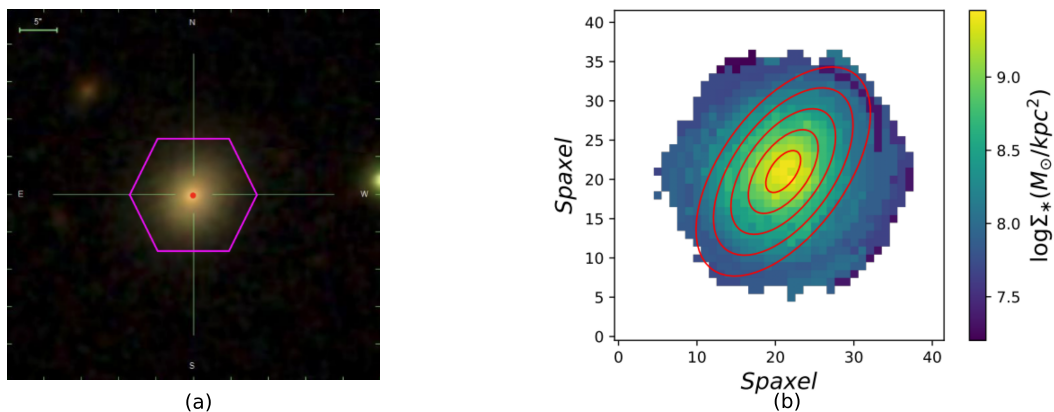


Fig. 2: The SDSS optical image of the target and the radial profile constructed on the stellar mass density map. a) SDSS g, r, i color image. b) Aperture drawn over the Σ_* map of galaxy PLATEIFU 11753-3701 in our sample. The ellipticity (ϵ) and position angle (PA) of the apertures are the same as those of this galaxy. The color is the value of each pixel and the color bar is the logarithmic display.

4. Results

4.1. Global properties

The different environments (i.e., formation pathways) will leave characteristic signatures in the newly formed S0s (e.g., Coccato et al. 2022). Figure 3a illustrates the distribution of the bulge Sérsic index derived from the Ser+Exp fit (Domínguez Sánchez et al. 2022) in the r-band for our samples. The Sérsic index values across our samples range from 0 to 8 (Gadotti 2009; Xiao et al. 2016; Coccato et al. 2022; Xu et al. 2022), with mean values of $2.37^{+0.31}_{-0.99}$ for SFS0s_HE and $1.77^{+0.63}_{-0.67}$ for SFS0s_LE. To compare the difference of Sérsic index distribution and the mean value of the two samples, we performed Kolmogorov-Smirnov test (KS_test) and Student's t-test (hereafter T_test) respectively (Table 2). The test results show that the two distributions are identical (KS_test: 0.08), and their mean values are also statistically consistent (T_test: 0.17). For the overall SFS0s (mean: $1.96^{+1.11}_{-0.85}$), the galaxies indeed demonstrate a higher incidence of pseudo bulges, consistent with the previous studies (e.g., Xu et al. 2022). If we truncate with Sérsic index = 2, we find that over 70% of galaxies in SFS0s_LE have Sérsic index < 2. However, the ratios of SFS0s_HE are close (Table 1).

Rathore et al. (2022) observed a pronounced reduction in the number of SFS0s beyond a stellar mass (M_*) threshold of 10.25 ($\log(M_*/M_\odot)$), suggesting a potential manifestation of mass-derived quenching. However, as they found, the relationship between mass quenching and SFS0s is unclear and requires further study of M_* and morphology, especially based on IFS data; however, we know that mass quenching does not depend on the galaxy's environment (e.g., Mao et al. 2022). In Fig. 3b, we present the M_* histogram, with mean values of $10.10^{+1.24}_{-0.60}$ (SFS0s_HE) and $10.15^{+0.48}_{-0.35}$ (SFS0s_LE). The KS_test and T_test both show that there is no difference between them (KS_test: 0.79; T_test: 0.17). For this reason, we do not discuss the effect of M_* in the subsequent analysis.

Furthermore, the size-mass relation (SMR) of galaxies serves as a valuable tool for exploring galaxy evolution (Cappellari et al. 2013; Cappellari 2016). Figure 3c displays the SMR, with R_e (r-band) measured in "kpc." We find a bend in this re-

Table 2: Global and derivative properties of our samples

Parameter	SFS0s_LE	SFS0s_HE	KS_test	T_test
(1)	(2)	(3)	(4)	(5)
Sérsic index	$1.77^{+0.63}_{-0.67}$	$2.37^{+0.31}_{-0.99}$	0.08	0.17
$\log M_*/M_\odot$	$10.15^{+0.48}_{-0.35}$	$10.10^{+1.24}_{-0.60}$	0.79	0.17
R_e (kpc)	$2.03^{+0.93}_{-0.74}$	$2.53^{+1.68}_{-0.54}$	0.28	0.57
B/T	$0.44^{+0.03}_{-0.14}$	$0.47^{+0.27}_{-0.21}$	0.35	0.62
$CI_{H\alpha}/\text{cont}$	$0.07^{+0.10}_{-0.25}$	$-0.04^{+0.27}_{-0.38}$	5×10^{-3}	0.01
$CI_{\text{SFR}, H\alpha}$	$2.34^{+0.22}_{-0.33}$	$1.99^{+0.09}_{-0.19}$	2×10^{-7}	2×10^{-3}

Notes: In this table, we represent each parameter as an average value with its FWHM of the distribution.

lation at the low-mass end, which may be due to a break in the SMR at $M_* \sim 3 \times 10^{10}$, known as a characteristic mass ("pivot mass;" e.g., Cappellari et al. 2013; Cappellari 2016; Mowla et al. 2019; Kawinwanichakij et al. 2021). This mass is considered to have physical significance as it is closer to the M_* threshold, beyond which 50% of galaxies are quenched (e.g., Mowla et al. 2019; Kawinwanichakij et al. 2021). Moreover, Cappellari et al. (2013) suggested that this bending corresponds to the two main formation pathways of ETGs. In Fig. 3c, we find that SFS0s_LE, on average, has slightly smaller R_e values (mean: $2.03^{+0.93}_{-0.74}$ kpc; $2.53^{+1.68}_{-0.54}$ kpc for SFS0s_HE). In other words, SFS0s_LE galaxies are more compact for a given M_* , although both tests show that there is no statistical difference in R_e (see Table 2). Table 1 provides a subdivision of our samples based on the M_* criterion from Rathore et al. (2022), presenting the proportions of high/low mass galaxies in our samples. Their proportions are also comparable. Figure 3d displays the histogram of the bulge-to-total light ratio (B/T). We find that the mean value of SFS0s_LE is $0.44^{+0.03}_{-0.14}$ and SFS0s_HE is $0.47^{+0.27}_{-0.21}$. The KS_test and T_test both indicate that there is no difference between them (KS_test: 0.35; T_test: 0.62). When considering our all samples (mean: $0.45^{+0.17}_{-0.11}$), this result is aligned with previous works.

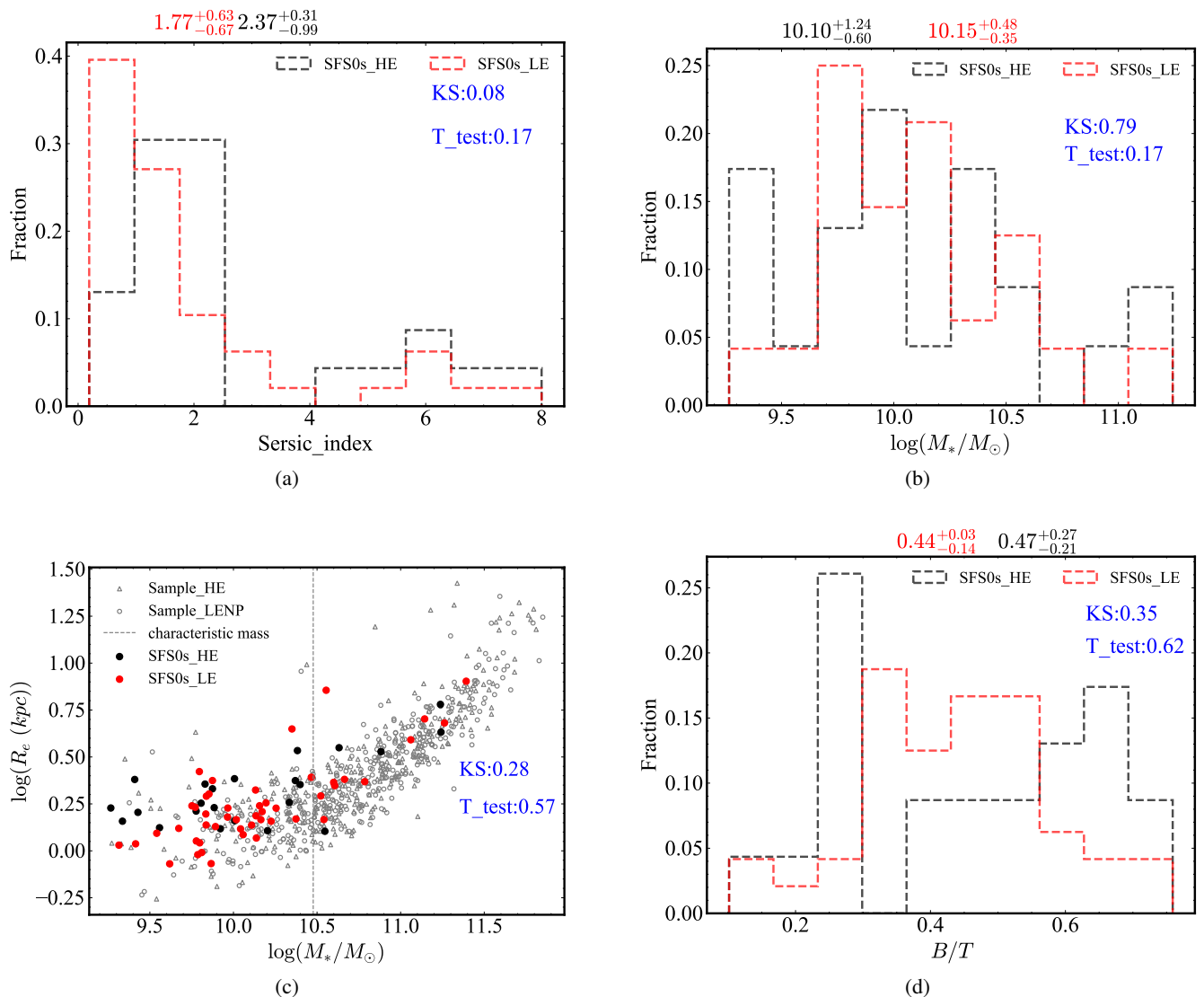


Fig. 3: The global properties of our two samples. a) Distributions of the bulges Sérsic index, which come from MaNGA_VAC photometrical catalog; b) Stellar mass (M_*) distribution; c) SMR. The gray dashed line represents the characteristic mass (“pivot mass”, $M_* \approx 3 \times 10^{10}$) of the SMR bend (Cappellari 2016; Mowla et al. 2019; Kawinwanichakij et al. 2021); In this figure, black and red circles represent our two samples and the rest are the same as Fig. 1; d) The bulge-to-total (B/T) light ratio distribution from Ser+Exp fit, which also comes from the photometrical catalog (r-band). In this picture, the top numbers represent the average of the parameters for our two samples, while the blue numbers in the picture represent different test results. The color markings are the same as in Fig. 1.

4.2. SFR CI

Previous studies have proposed various morphological parameters to distinguish between ETGs and LTGs (e.g., Huertas-Company et al. 2009; Mahoro et al. 2019; Bignone et al. 2020), where the concentration index (CI) describes the distribution of light among the associated pixels within a galaxy (Abraham et al. 1996; Bershadsky et al. 2000; Abraham et al. 2003; Lotz et al. 2004). Wang et al. (2022) used the concentrated SF and stellar population (SP) ages to study the effects of environmental quenching on all galaxies in the SAMI Survey. They defined their CI parameter ($CI_{H\alpha/\text{cont}}$) of the gas disk relative to the stellar disk:

$$CI_{H\alpha/\text{cont}} = \log(r_{50,H\alpha}/r_{50,\text{cont}}) \quad (8)$$

where “cont” refers to the r -band continuum of their galaxies and r_{50} represents the radius containing 50% of the emission line or continuum luminosity. In Figure 4, we give the distributions of $CI_{H\alpha/\text{cont}}$, where blue numbers represent the test (KS_test and T_test) of $CI_{H\alpha/\text{cont}}$ distributions and mean values, and black and red numbers are the mean values of $CI_{H\alpha/\text{cont}}$. We find that the $CI_{H\alpha/\text{cont}}$ is larger ($0.07^{+0.10}_{-0.25}$) in SFS0s_LE and smaller in SFS0s_HE ($-0.04^{+0.27}_{-0.38}$). The KS_test shows that the difference of the $CI_{H\alpha/\text{cont}}$ parameter is statistically significant (KS_test: 5×10^{-3}), and their means are also inconsistent (T_test: 0.01). In other words, the distributions of gas in SFS0s on the gas disk are different in different environments. Of course, the variation in the gas disk present in the two samples relative to the stellar disk can be called the shrinking effect of the gas disk. Previous findings indicate that the H I disk of a galaxy responds to rem-

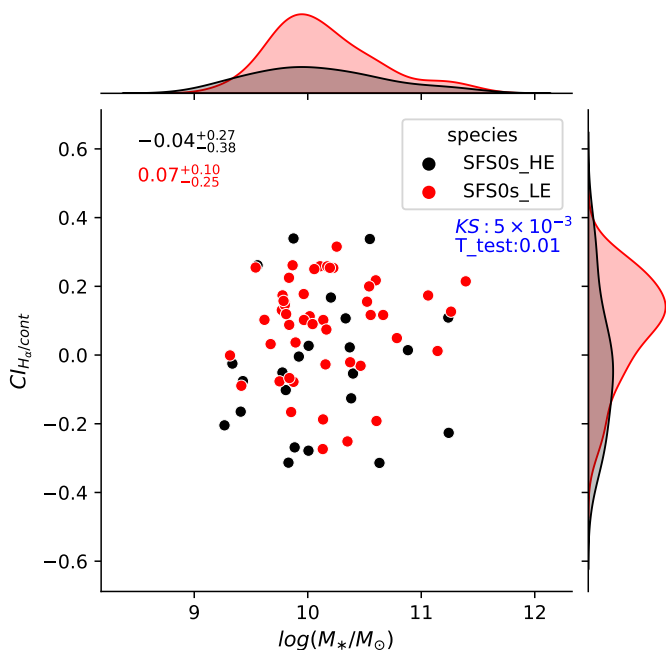


Fig. 4: $CI_{H\alpha}/cont$ values based on the concentration defined (Formula 8) from Wang et al. (2022) (black: SFS0s_HE; red: SFS0s_LE). The mean $CI_{H\alpha}/cont$ of galaxies in HDEs and LDEs is $-0.04^{+0.27}_{-0.38}$ and $0.07^{+0.10}_{-0.25}$, respectively. The curves on the top and right illustrate the distributions of the parameters on the horizontal and vertical coordinates. The KS_test and T_test results are represented by the blue numbers.

pressure stripping (RPS) by shrinking (Lin et al. 2023), while the stellar disk remains unaffected.

The two origin mechanisms proposed above make the disturbance of the gas and stars of the galaxy different in different environments (e.g., Deeley et al. 2020, 2021; Boselli et al. 2022). Thus, we only focus on the gas disk of the galaxy to prove the difference in $CI_{H\alpha}/cont$ parameter. Bershadsky et al. (2000) provided the concentration index (CI), which is defined as the logarithm of the ratio of the circular radii containing 80% and 20% of the total flux (Bershadsky et al. 2000):

$$CI = 5 \times \log(R_{80}/R_{20}) \quad (9)$$

Typically, higher CI values correspond to higher fractions of light in the central regions, suggesting that the galaxy is less disturbed (Getachew-Woreta et al. 2022). In the case of our SFS0s, we apply the CI (formula 9) to analyze the SFR of these galaxies ($CI_{SFR,H\alpha}$). Specifically, we define this parameter as the logarithm of the ratio of the circular radii containing 80% and 20% of the total SFR of star-forming pixels within the galaxy:

$$CI_{SFR,H\alpha} = 5 \times \log(R_{80,SFR}/R_{20,SFR}) \quad (10)$$

The CI parameter (formula 9) is originally associated with the stellar continuum, but in this context, we adapt it (formula 10) to assess the distribution of ionized gas in galaxies, specifically the distribution of $H\alpha$ emission. This adaptation assumes elliptical or circular distributions of $H\alpha$. By examining the $H\alpha$ emission, we find that the fraction of galaxies in our sample that exhibit significant clumps is negligible. Moreover, galaxies with star-forming rings (e.g., Boselli et al. 2022; Tous et al.

2023) are only a few percent of our sample, and therefore do not have a noticeable impact on the analysis of $CI_{SFR,H\alpha}$, even though such ring structures are quite common in SFS0s (Boselli et al. 2022). The distributions of $CI_{SFR,H\alpha}$ are depicted in Figure 5a, while the Cumulative distribution functions (CDF) are illustrated in Figure 5b. The color markings in both figures correspond to those in Figure 1. We find that the $CI_{SFR,H\alpha}$ parameter is larger in SFS0s_LE (mean: $2.34^{+0.22}_{-0.33}$) and smaller in SFS0s_HE ($1.99^{+0.09}_{-0.19}$). We provide the results of KS_test and T_test (blue numbers) for $CI_{SFR,H\alpha}$ parameter in this figure. We find that the $CI_{SFR,H\alpha}$ difference between the two samples is statistically significant (KS_test: 2×10^{-7}), and their means also show significant differences (T_test: 2×10^{-3}). Also, the CDF can tell us the same result (Figure 5b).

4.3. Radial profiles of derived quantities

In Fig. 6a, a noticeable central peak of Σ_{SFR} in both samples is observed, gradually diminishing with increasing radial distance. To depict the efficiency of gas conversion into stars within a galaxy, we present radial profiles of rsSFR in Fig. 6b. This pattern is aligned with previous findings, such as the study by Rathore et al. (2022), where it was suggested that their primary SF activities predominantly occur in the inner regions (Sect. 4.2). Moreover, this also indicates that potential contamination (about 8%) from SGs are not expected to affect our results. We find that the radial profiles of Σ_{SFR} and rsSFR for the two samples are different and even when we consider the error bars, there is no overlap between the two quantities. For LDEs, both quantities are higher than HDEs, but there is a more pronounced steepness in HDEs.

As mentioned above, different perturbations of SFS0s in different environments have different effects on the gas and star in the system ($CI_{H\alpha}/cont$; Fig. 4). This leads to a distinct difference in the distribution of SF in the galaxy, as traced by the concentration indices of SFR ($CI_{SFR,H\alpha}$; Figs. 4 and 5a). These characteristics are bound to affect the distribution of D_n4000 in SFS0s. In Fig. 7a, we provide the D_n4000 radial profiles, which are the SP age gradients in different environments. We find that the SPs' age of the galaxy in HDEs increases with the increase of radial distance, which corresponds to the younger bulges and the older disk (Johnston et al. 2012); whereas it appears to be flatter in SFS0s_LE. Furthermore, The SPs in LDEs are younger than that in HDEs.

According to Sect. 3.3, we employed the ($[O II] \lambda\lambda 3726, 3729 + [O III] \lambda\lambda 4959, 5007$)/ $H\beta$ (R_{23} , S/N of these lines ≥ 3) ratio as a tracer of the gas-phase metallicity (Tremonti et al. 2004; Bao et al. 2021) and the results are shown in Fig. 7b. The observed trend in our samples reveals a gradual decline in metallicity from the inner to outer regions, consistent with previous results (e.g., Cao et al. 2022; Smirnova-Pinchukova et al. 2022). We find that the changing trends of the two are very similar and very closely aligned.

5. Discussion

We find no statistical difference in the bulge Sérsic index, stellar mass, and B/T ratio among our two samples in Sect. 4.1. In addition, the T_test also shows no difference in their mean values (Table 2). Combined with the size of our sample and the fact that SFS0s only represent a very specific phase in the transition from gas-rich SGs to gas-poor S0s, we consider these results normal. When we consider these parameters of the total sample, it is consistent with previous works: contains more pseudo-

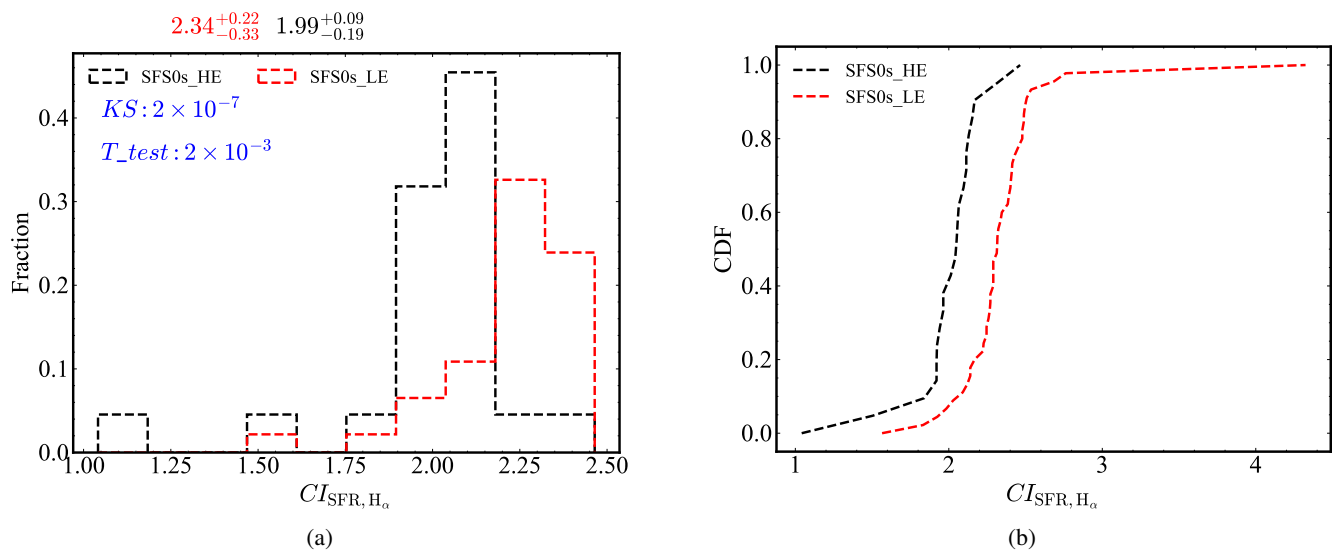


Fig. 5: $CI_{SFR,H\alpha}$ distributions and its Cumulative distribution function (CDF). a) $CI_{SFR,H\alpha}$ distributions. The blue numbers represent the results of the KS_test and T_test, and the different color numbers are the mean value of the two samples; b) The CDF of the $CI_{SFR,H\alpha}$. Color markings are the same as in Figure 1.

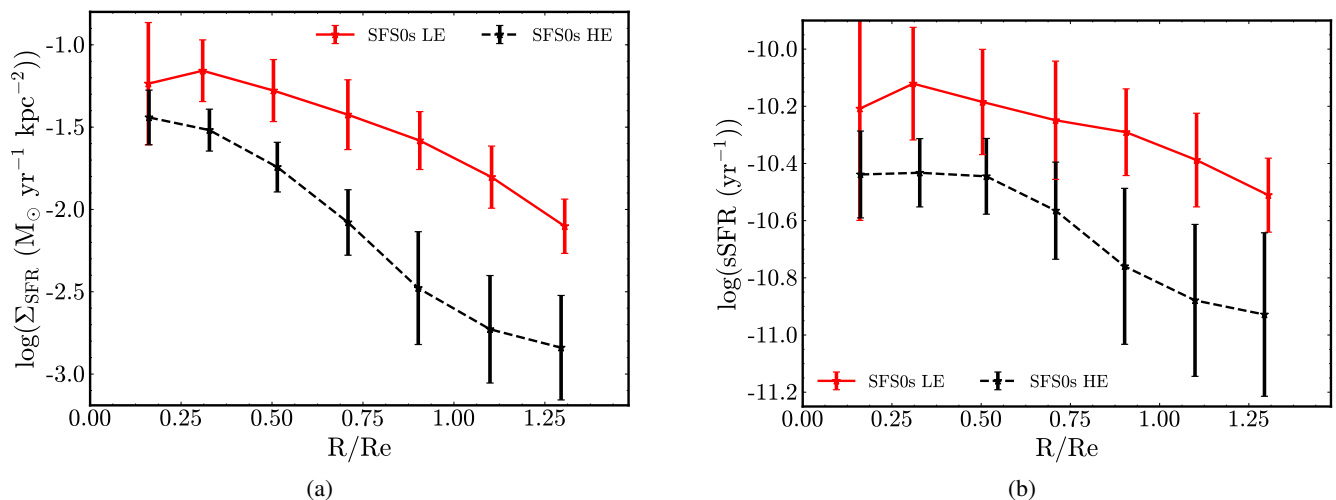


Fig. 6: The radial profiles of Σ_{SFR} and $rsSFR$. a) Σ_{SFR} radial profiles; b) $rsSFR$ radial profiles. Color markings of our samples are the same as in Figure 1. The error bars represent the standard deviation.

bulges, smaller B/T ratios, and similar M_* (e.g., Xiao et al. 2016; Vázquez-Mata et al. 2022; Xu et al. 2022). We also find the bending on the SMR (e.g., Cappellari et al. 2013; Cappellari 2016). In contrast, Coccato et al. (2022) combined kinematics, morphology, and properties of the stellar populations (SPs) of 329 S0s from SAMI/MaNGA to study the role of environment in the formation and evolution of S0s. These authors found that the sub-sample originating from the “faded spiral” was (on average) younger, more rotationally supported, smaller, and with lower Sérsic index, less massive, and tended to have slightly smaller B/T values. However, the sub-sample originating from the “merger” was older, more pressure supported, larger, and with larger Sérsic index, more massive, and tended to be slightly higher B/T. The difference between our results and Coccato et al. (2022) may be due to our sample is all S0s in the star-forming state (see Tables A.1 and A.2) and it may be found that the distribution of SFR in our sample is different from theirs (refer to their Table 1).

We provide the CI parameters ($CI_{H\alpha/cont}$ and $CI_{SFR,H\alpha}$) of the galaxy’s SF in Sect. 4.2 to reflect the influence of the environment on the distribution of galaxy’s SF. We find that the difference in $CI_{H\alpha/cont}$ between the two samples is significant (KS_test: 5×10^{-3} ; T_test: 0.01) and can be attributed to different origin mechanisms in different environments. The origin of galaxies in SFS0s_LE originates from: a minor merger, with the merger or inflow of fresh external gas (e.g., Katkov et al. 2014), which leads to a more extended distribution of gas in these galaxies compared to stellar disks. However, galaxies in SFS0s_HE experience gas stripping, losing gas from the outer disk (RPS; Vollmer 2013; Boselli et al. 2022), or a blocking of the external gas supply (starvation/strangulation; Boselli et al. 2006, 2016; Fossati et al. 2018; Boselli et al. 2022). This results in a more compact distribution of gas compared to stellar disks (see Fig. 4), which has been confirmed by the shrinking effect of the H I disk reported in a previous work (Lin et al. 2023). There-

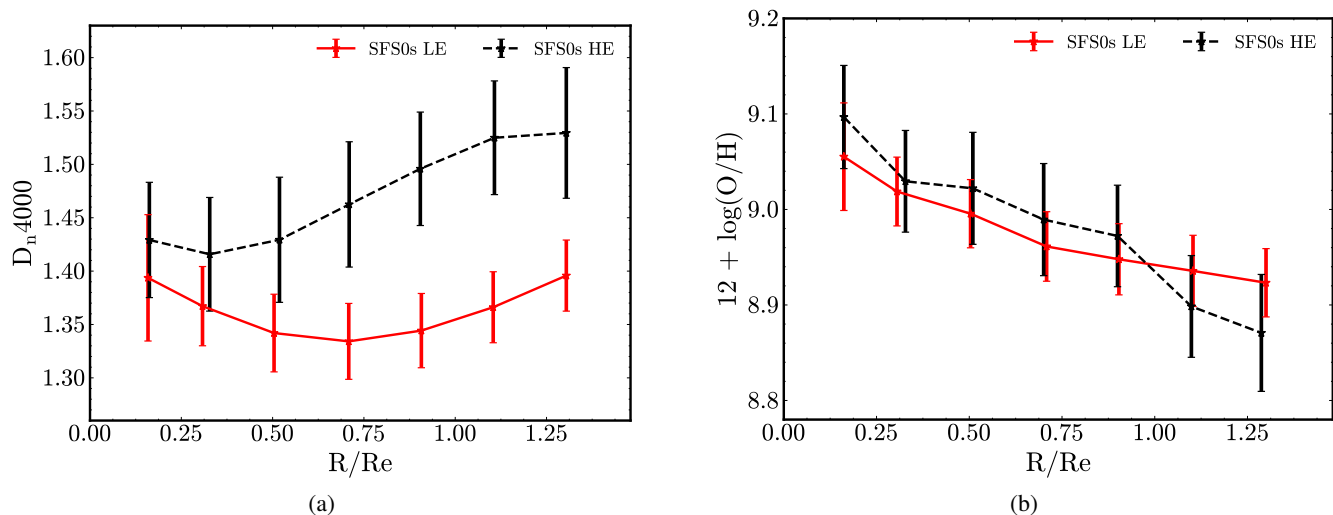


Fig. 7: The radial profiles of D_n4000 and gas-phase metallicity. a) D_n4000 radial profiles; b) Gas-phase metallicity radial profiles. The color markings are the same as in Figure 1. The error bars represent the standard deviation.

fore, SFS0s exhibits a larger $CI_{H\alpha}/cont$ ($0.07^{+0.10}_{-0.25}$) in SFS0s_LE, while SFS0s_HE exhibits a smaller $CI_{H\alpha}/cont$ ($-0.04^{+0.27}_{-0.38}$).

To confirm this discrepancy, we referred to the CI parameters of light within galaxies and defined a $CI_{SFR,H\alpha}$ parameter that only considers the gas disk in the galaxy. Combining the meaning of $CI_{H\alpha}/cont$, the gas disk in SFS0s_HE produces a shrinking effect (Lin et al. 2023), and these galaxies either lose gas from the outer disk or have no external gas supply. Therefore, the SF of these galaxies is either truncated or uniformly stopped after consuming gas reservoir (Boselli et al. 2006, 2016; Fossati et al. 2018; Boselli et al. 2022). However, the SFS0s_LE can have a supply of external gas and even fall into the nuclear regions of the galaxy (Kewley & Dopita 2002; Hwang et al. 2019), so the SF of the outer regions for these galaxies may be high in comparison, depending on the angular momentum of the gas reaching the outer disk of the galaxy (Hao et al. 2019). Therefore, the galaxies in SFS0s_LE exhibit higher $CI_{SFR,H\alpha}$ ($2.34^{+0.22}_{-0.33}$), while SFS0s_HE shows lower parameter ($1.99^{+0.09}_{-0.19}$). The difference is statistically significant (KS_test: 2×10^{-7} and T_test: 2×10^{-3}). By comparing the $R_{80,SFR}$ (SFS0s_LE median: 3.00 kpc; SFS0s_HE: 2.48 kpc) and R_e of our galaxies with stellar mass smaller than the “pivot mass,” we are able to obtain similar results. The consistency between the $R_{20,SFR}$ (SFS0s_LE median: 0.76 kpc; SFS0s_HE: 0.59 kpc; KS_test: 0.13) of the two samples also seems to indicate that the SF of these SFS0s is center-dominated rather than disk-dominated (Rathore et al. 2022). It is crucial to emphasize that our application of $CI_{SFR,H\alpha}$ only considers the gas disk of the galaxy, excluding the stellar disk. Certainly, further validation through observations or simulations that demonstrate changes in the gas gradient on the gas disks of galaxies subjected to perturbed processes would enhance the credibility of our findings. However, it is disappointing that no consensus has been reached so far. Ongoing advancements in observational techniques and simulation capabilities could potentially shed more light on these aspects, contributing to a deeper understanding of the relationship between environments, perturbation processes, and gas distribution in galaxies.

Here, we find that there are obvious differences in the SF distributions of SFS0s in different environments, so we further study the radial profile of the galaxy’s derivation quanti-

ties. In Fig. 6, we find that on average, SFS0s_LE has a higher $\Sigma_{SFR}/rsSFR$, which is attributed to the injection of fresh external gas. These newly entered gases may not immediately participate in SF, only igniting the SF of the galaxy when the gas loses its original angular momentum and cooling (Hao et al. 2019). This is consistent with the origin of the “minor merger.” However, the disturbance mechanisms of SFS0s_HE either force the gas in the outer disk to be stripped or stop the supply of gas for the galaxy, so a low $\Sigma_{SFR}/rsSFR$ is understandable. This is consistent with a “faded spiral” origin. Of course, to confirm this result requires testing the content of atomic or molecular gas in SFS0s (Chen et al in prep). In addition, the central peak Σ_{SFR} of both samples does indicate that their SF activities are concentrated in the galaxy’s center (Rathore et al. 2022).

It is precisely thanks to the different origin mechanisms that we have discovered differences in SP ages (D_n4000 ; see Fig. 7a). As mentioned earlier, the merger-like events experienced by galaxies in LDEs involve the merging or inflow of external gas (e.g., Katkov et al. 2014), even forcing this gas to fall into the galaxy’s nuclear regions (Kewley & Dopita 2002; Hwang et al. 2019). The dissipation of angular momentum (Hao et al. 2019) and the cooling of the gas during the fall will ignite the SF of the corresponding regions, resulting in the formation of young massive stars in these regions; thus, their SP ages will be slightly younger (lower D_n4000). For the SFS0s_HE sample, however, the galaxy undergoes a perturbation process that either causes the galaxy to preferentially lose gas from the outer disk or prevents the supply of external gas, thereby demonstrating a gradually increasing D_n4000 value (e.g., Lee et al. 2022; Loni et al. 2023). The change in the SP age gradient in SFS0s_HE seems to correspond to an outside-in quenching mechanism (Fossati et al. 2018; Lin et al. 2019).

However, what was most surprising was the fact that the origin mechanism of SFS0s_LE requires the presence of external fresh gas merging or inflow. These metal-poor gases from CGM, IGM, companion or satellite galaxies (Kewley & Dopita 2002; Hwang et al. 2019) will significantly dilute the gas phase metallicity of the galaxy (Ellison et al. 2008; Kewley et al. 2010). In contrast, we did not find any significantly lower gas-phase metallicity in SFS0s_LE (see Fig. 7b). After the gas in the outer disk of the galaxy is stripped away, it will leave behind obvious metal-

rich systems (Hughes et al. 2013). However, we did not find any increased metallicity in SFS0s_HE either. As described in Sect. 4.1, although the R_e of the two samples follows the same statistical distribution, we can observe that the galaxies in SFS0s_LE have on average smaller sizes, especially those below the “pivot mass,” which leads to higher gravitational potential ($\Phi \propto M_*/R_e$, Vaughan et al. 2022). Therefore, the feedback processes present in galaxies may not be sufficient to remove metals from such systems (e.g., Cairós & González-Pérez 2020), leading to an increase in metallicity in SFS0s_LE. In fact, the gas-phase metallicity is the result of competition between gas inflow, outflow, supernova feedback, and SF feedback. It is only when the inflow of metal-poor gas is strong and the SF does not last long enough to enrich the interstellar medium (ISM) through supernova explosions, the galaxy may exhibit metallicity deficiency (Hao et al. 2024). In the studies of Cao et al. (2022) and Hao et al. (2024), no significantly lower metallicity was found in systems that may have the external fresh gas supply. Of course, we checked SFS0s of different M_* and excluded the influence of M_* , which gave the same result. Moreover, using the measurements from the central $3''$ within galaxies provided by MPA-JHU (Tremonti et al. 2004), we also observed the same result. Previous works have shown that gas-rich galaxies in rich environments have, on average, higher metallicity than their counterparts in sparse environments (Shields et al. 1991; Hughes et al. 2013). Similarly, this requires testing the gas content in these galaxies (Chen et al in prep).

Of course, it is worth noting how frequently these disturbance mechanisms exist in different environments within the M_* range and redshift range of our sample. Because studies have found that the merging fraction varies significantly with redshift and the M_* of galaxies (e.g., Lotz et al. 2011). Nevin et al. (2023) studied 1.3 million galaxies from the SDSS DR16 photometric catalog and presented the probability that each galaxy is a major or minor merger, splitting the classifications into merger stages (early, late, and post-coalescence). They found that the fraction of minor merger occurring in massive galaxies ($\log M_* \geq 10.40 M_\odot$) is approximately 20% - 65% at redshift $z \sim 0.01-0.05$, while the fraction of major merger occurring is approximately 10% - 30% ($z = 0-0.05$) when the M_* is not considered. If we assume that all the galaxies in the sample SFS0s_LE come from the merger, then this fraction (68%, 48/71, or massive fraction 21%, 15/71) is consistent. In addition, simulations (Yun et al. 2019) have shown that galaxies affected by RPS are common in galaxy clusters with a redshift $z < 0.6$, with approximately 30% of disk galaxies having gas compositions resembling comet shapes (Boselli et al. 2019). Indeed, if we assume that all galaxies in SFS0s_HE come from RPS, then this frequency is also consistent (32%, 23/71). However, it is important to note that due to the size and specificity of our sample, we cannot draw any firm conclusions, therefore these results ought to be taken with caution.

6. Conclusions

We assembled a sample of 71 SFS0s, utilizing data from the SDSS-IV MaNGA survey and subsequently segregating it into two categories based on environmental density information: SFS0s_HE (23 galaxies) and SFS0s_LE (48 galaxies). Our analysis comprises a comparison of global properties (e.g., Sérsic index, B/T) between the two samples. Subsequently, we computed the CI parameters ($CI_{H\alpha/\text{cont}}$ and $CI_{\text{SFR},H\alpha}$), followed by the construction of radial profiles for derived quantities of galax-

ies (e.g., rsSFR, D_n4000). The key outcomes of our investigation are outlined below.

- By comparing the global properties of the two samples, we suggest that different environments do not significantly affect them. These properties changes in the total sample are consistent with previous works. Furthermore, the difference in these properties from Coccato et al. (2022) should be attributed to the different distribution of the SFR. This population is special and rare, which may only represent a very special phase in the transition from gas-rich SGs to gas-poor S0s.
- The dominant perturbation processes in different environments have different effects on the gas and stars in the galaxy, so we first consider the $CI_{H\alpha/\text{cont}}$ parameter that includes the stellar and gas of the galaxy. We find that HDEs show a smaller $CI_{H\alpha/\text{cont}}$, while LDEs show a larger $CI_{H\alpha/\text{cont}}$. This is because the inflow of fresh gas from outside causes the distribution of gas in SFS0s_LE to be more extended compared to the stellar disk. Galaxies that are subject to disturbances similar to RPS will experience the shrinking effect of H I disk (Lin et al. 2023). To confirm this result, we used $CI_{\text{SFR},H\alpha}$, a parameter that only considers the gas disk of the galaxy. We find that it is indeed the merging or inflow of external gas in LDEs that causes the $CI_{\text{SFR},H\alpha}$ value to be larger, while the stripping of gas in HDEs makes it smaller. We note that these differences are statistically significant.
- We constructed radial profiles of some quantities (Σ_{SFR} , rsSFR, D_n4000 , and gas-phase metallicity). We find that, on average, SFS0s_LE has a higher $\Sigma_{\text{SFR}}/\text{rsSFR}$, which is attributed to the injection of fresh external gas. These newly entered gases may not immediately participate in SF, only igniting the SF of the galaxy when the gas loses its original angular momentum and cooling (Hao et al. 2019). This is consistent with the origin mechanism of a “minor merger.” However, the disturbance mechanisms of SFS0s_HE either force the gas in the outer disk to be stripped or stop the supply of gas for the galaxy, so a low $\Sigma_{\text{SFR}}/\text{rsSFR}$ is understandable. This is consistent with the “faded spiral” origin. In addition, the central peak Σ_{SFR} of both samples does indicate that their SF activities are concentrated in the galaxy’s center.
- We find that it may be due to the inflow of external fresh gas into SFS0s_LE that they have a lower and relatively flat age gradient of SPs (i.e., D_n4000), while gas stripping or cessation of gas supply leads to a gradually increasing age gradient in SFS0s_HE. This difference corresponds well to their different origin mechanisms. Most of this fresh gas from the outside is metal-poor, but we do not find a significantly lower gas-phase metallicity in SFS0s_LE. The inspection of the measurements from the central $3''$ within galaxies provided by MPA-JHU and the M_* both show the same results. In fact, the gas-phase metallicity is the result of competition between gas inflow, outflow, supernova feedback, and SF feedback. It is only when the inflow of metal-poor gas is strong and SF does not last long enough to enrich the interstellar medium (ISM) through supernova explosions that the galaxy may exhibit a metallicity deficiency.

It is important to note that the results presented here are based on our analysis of SFS0s from the SDSS-IV MaNGA Survey. The fraction of high- and low-mass galaxies within our subsample is fairly balanced. However, given the relatively small total sample size (71), future investigations ought to explore the

potential impact of M_* on the SFSOs population. Considering the size of our sample and the unique nature of SFSOs, additional atomic and molecular gas data may provide a better understanding of this work (Chen et al. 2023; Loni et al. 2023). Deep H I data, for instance, prove valuable in unraveling the historical and ongoing effects of gravitational and hydrodynamic processes, especially in transitioning galaxies from LDEs to HDEs (Loni et al. 2023). Most importantly, atomic and molecular gas data can help us answer some of the questions above and potentially determine the position of blue ETGs (e.g., SFSOs) in the overall evolutionary picture (Chen et al in prep). Furthermore, exploring feedback processes in S0s, such as AGN feedback, as well as understanding the progenitors (e.g., passive and red SGs, Pak et al. 2019; Zhou et al. 2021) of these galaxies, is still of interest. The existence of passive and red SGs serves as compelling evidence for the morphological transformation of SGs into S0s, particularly in galaxy groups or rich galaxy clusters (e.g., Pak et al. 2019).

Acknowledgements. We are grateful to the anonymous referee for her/his thoughtful review and very constructive suggestions, which greatly improved this paper. We thank Dr. Qiusheng Gu and Dr. Min Du for the helpful discussion on related observations and simulations. J.W. acknowledges the National Key R&D Program of China (Grant No. 2023YFA1607904) and the National Natural Science Foundation of China (NSFC) grants 12033004, 12221003, 12333002 and the science research grant from CMS-CSST-2021-A06. T.C. acknowledges the China Postdoctoral Science Foundation (Grant No. 2023M742929). This research made use of Photutils, an Astropy package for detection and photometry of astronomical sources (Bradley et al. 2022). Funding for the Sloan Digital Sky Survey IV has been provided by the Alfred P. Sloan Foundation, the U.S. Department of Energy Office of Science, and the Participating Institutions. SDSS-IV acknowledges support and resources from the Center for High-Performance Computing at the University of Utah. The SDSS website is www.sdss.org. SDSS-IV is managed by the Astrophysical Research Consortium for the Participating Institutions of the SDSS Collaboration including the Brazilian Participation Group, the Carnegie Institution for Science, Carnegie Mellon University, the Chilean Participation Group, the French Participation Group, Harvard-Smithsonian Center for Astrophysics, Instituto de Astrofísica de Canarias, The Johns Hopkins University, Kavli Institute for the Physics and Mathematics of the Universe (IPMU) / University of Tokyo, Lawrence Berkeley National Laboratory, Leibniz Institut für Astrophysik Potsdam (AIP), Max-Planck-Institut für Astronomie (MPIA Heidelberg), Max-Planck-Institut für Astrophysik (MPA Garching), Max-Planck-Institut für Extraterrestrische Physik (MPE), National Astronomical Observatory of China, New Mexico State University, New York University, University of Notre Dame, Observatório Nacional / MCTI, The Ohio State University, Pennsylvania State University, Shanghai Astronomical Observatory, United Kingdom Participation Group, Universidad Nacional Autónoma de México, University of Arizona, University of Colorado Boulder, University of Oxford, University of Portsmouth, University of Utah, University of Virginia, University of Washington, University of Wisconsin, Vanderbilt University, and Yale University. Facilities: Sloan Software: astropy [Astropy Collaboration et al. \(2013, 2018, 2022\)](https://www.astropy.org); Tool for Operations on Catalogues And Tables (TOPCAT; Taylor 2005)

References

Abdurro'uf, Accetta, K., Aerts, C., et al. 2022, *ApJS*, 259, 35
 Abraham, R. G., van den Bergh, S., Glazebrook, K., et al. 1996, *ApJS*, 107, 1
 Abraham, R. G., van den Bergh, S., & Nair, P. 2003, *ApJ*, 588, 218
 Aird, J., Coil, A. L., Moustakas, J., et al. 2012, *ApJ*, 746, 90
 Aragon-Salamanca, A., Baugh, C. M., & Kauffmann, G. 1998, *MNRAS*, 297, 427
 Argudo-Fernández, M., Verley, S., Bergond, G., et al. 2015, *A&A*, 578, A110
 Astropy Collaboration, Price-Whelan, A. M., Lim, P. L., et al. 2022, *ApJ*, 935, 167
 Astropy Collaboration, Price-Whelan, A. M., Sipőcz, B. M., et al. 2018, *AJ*, 156, 123
 Astropy Collaboration, Robitaille, T. P., Tollerud, E. J., et al. 2013, *A&A*, 558, A33
 Bait, O., Barway, S., & Wadadekar, Y. 2017, *MNRAS*, 471, 2687
 Baldwin, J. A., Phillips, M. M., & Terlevich, R. 1981, *PASP*, 93, 5
 Balogh, M., Eke, V., Miller, C., et al. 2004, *MNRAS*, 348, 1355
 Bao, M., Chen, Y., Yuan, Q., et al. 2021, *MNRAS*, 505, 191
 Barway, S., Wadadekar, Y., Kembhavi, A. K., & Mayya, Y. D. 2009, *MNRAS*, 394, 1991

Barway, S., Wadadekar, Y., Vaghmare, K., & Kembhavi, A. K. 2013, *MNRAS*, 432, 430
 Bershady, M. A., Jangren, A., & Conselice, C. J. 2000, *AJ*, 119, 2645
 Bignone, L. A., Pedrosa, S. E., Trayford, J. W., Tissera, P. B., & Pellizza, L. J. 2020, *MNRAS*, 491, 3624
 Blanton, M. R., Bershady, M. A., Abolfathi, B., et al. 2017, *AJ*, 154, 28
 Blanton, M. R., Kazin, E., Muna, D., Weaver, B. A., & Price-Whelan, A. 2011, *AJ*, 142, 31
 Bluck, A. F. L., Maiolino, R., Piotrowska, J. M., et al. 2020, *MNRAS*, 499, 230
 Boselli, A., Boissier, S., Cortese, L., et al. 2006, *ApJ*, 651, 811
 Boselli, A., Epinat, B., Contini, T., et al. 2019, *A&A*, 631, A114
 Boselli, A., Fossati, M., Longobardi, A., et al. 2022, *A&A*, 659, A46
 Boselli, A. & Gavazzi, G. 2006, *PASP*, 118, 517
 Boselli, A., Roehly, Y., Fossati, M., et al. 2016, *A&A*, 596, A11
 Bradley, L., Sipőcz, B., Robitaille, T., et al. 2022, *astropy/photutils: 1.6.0*, Zenodo
 Bundy, K., Bershady, M. A., Law, D. R., et al. 2015, *ApJ*, 798, 7
 Cairós, L. M. & González-Pérez, J. N. 2020, *A&A*, 634, A95
 Calzetti, D. 2001, *PASP*, 113, 1449
 Cao, X., Chen, Y.-M., Shi, Y., et al. 2022, *Nature Astronomy*, 6, 1464
 Cappellari, M. 2016, *ARA&A*, 54, 597
 Cappellari, M., McDermid, R. M., Alatalo, K., et al. 2013, *MNRAS*, 432, 1862
 Cattorini, F., Gavazzi, G., Boselli, A., & Fossati, M. 2023, *A&A*, 671, A118
 Chen, P., Zhao, Y., & Wang, J. 2023, *Research in Astronomy and Astrophysics*, 23, 015005
 Coccatto, L., Fraser-McKelvie, A., Jaffé, Y. L., et al. 2022, *MNRAS*, 515, 201
 Coccatto, L., Jaffé, Y. L., Cortesi, A., et al. 2020, *MNRAS*, 492, 2955
 Davis, T. A., Young, L. M., Crocker, A. F., et al. 2014, *MNRAS*, 444, 3427
 Deeley, S., Drinkwater, M. J., Sweet, S. M., et al. 2021, *MNRAS*, 508, 895
 Deeley, S., Drinkwater, M. J., Sweet, S. M., et al. 2020, *MNRAS*, 498, 2372
 Diaz, J., Bekki, K., Forbes, D. A., et al. 2018, *MNRAS*, 477, 2030
 Domínguez Sánchez, H., Huertas-Company, M., Bernardi, M., Tuccillo, D., & Fischer, J. L. 2018, *MNRAS*, 476, 3661
 Domínguez Sánchez, H., Margalef, B., Bernardi, M., & Huertas-Company, M. 2022, *MNRAS*, 509, 4024
 Donzelli, C. J., Muriel, H., & Madrid, J. P. 2011, *ApJS*, 195, 15
 Dressler, A. 1980, *ApJ*, 236, 351
 Dressler, A., Oemler, Augustus, J., Couch, W. J., et al. 1997, *ApJ*, 490, 577
 Dressler, A., Oemler, Augustus, J., Poggianti, B. M., et al. 2004, *ApJ*, 617, 867
 Eliche-Moral, M. C., Rodríguez-Pérez, C., Borlaff, A., Querejeta, M., & Tapia, T. 2018, *A&A*, 617, A113
 Ellison, S. L., Patton, D. R., Simard, L., & McConnachie, A. W. 2008, *AJ*, 135, 1877
 Ellison, S. L., Sánchez, S. F., Ibarra-Medel, H., et al. 2018, *MNRAS*, 474, 2039
 Etherington, J. & Thomas, D. 2015, *MNRAS*, 451, 660
 Forbes, D. A., Spitler, L. R., Strader, J., et al. 2011, *MNRAS*, 413, 2943
 Fossati, M., Mendel, J. T., Boselli, A., et al. 2018, *A&A*, 614, A57
 Fraser-McKelvie, A., Aragón-Salamanca, A., Merrifield, M., et al. 2018, *MNRAS*, 481, 5580
 Gadotti, D. A. 2009, *MNRAS*, 393, 1531
 Getachew-Woreta, T., Pović, M., Masegosa, J., et al. 2022, *MNRAS*[arXiv:2203.07702]
 Gunn, J. E. & Gott, J. Richard, I. 1972, *ApJ*, 176, 1
 Hao, C.-N., Shi, Y., Chen, Y., et al. 2019, *ApJ*, 883, L36
 Hao, C.-N., Xia, X., Shi, Y., et al. 2024, *ApJ*, 968, 3
 Hubble, E. P. 1936, in *Realm of the Nebulae*, ed. E. P. Hubble (New Haven: Yale Univ. Press), 45
 Huertas-Company, M., Tasca, L., Rouan, D., et al. 2009, *A&A*, 497, 743
 Hughes, T. M., Cortese, L., Boselli, A., Gavazzi, G., & Davies, J. I. 2013, *A&A*, 550, A115
 Hwang, H.-C., Barrera-Ballesteros, J. K., Heckman, T. M., et al. 2019, *ApJ*, 872, 144
 Johnston, E. J., Aragón-Salamanca, A., Merrifield, M. R., & Bedregal, A. G. 2012, *MNRAS*, 422, 2590
 Johnston, E. J., Häußler, B., Jegatheesan, K., et al. 2022, *MNRAS*, 514, 6141
 Kannappan, S. J., Guie, J. M., & Baker, A. J. 2009, *AJ*, 138, 579
 Katkov, I. Y., Sil'chenko, O. K., & Afanasiev, V. L. 2014, *MNRAS*, 438, 2798
 Kauffmann, G., Heckman, T. M., Tremonti, C., et al. 2003, *MNRAS*, 346, 1055
 Kawinwanichakij, L., Silverman, J. D., Ding, X., et al. 2021, *ApJ*, 921, 38
 Kennicutt, Robert C., J. 1998, *ARA&A*, 36, 189
 Kewley, L. J. & Dopita, M. A. 2002, *ApJS*, 142, 35
 Kewley, L. J., Dopita, M. A., Sutherland, R. S., Heisler, C. A., & Trevena, J. 2001, *ApJ*, 556, 121
 Kewley, L. J., Rupke, D., Zahid, H. J., Geller, M. J., & Barton, E. J. 2010, *ApJ*, 721, L48
 Kolcu, T., Crossett, J. P., Bellhouse, C., & McGee, S. 2022, *MNRAS*, 515, 5877
 Kormendy, J. & Bender, R. 2012, *ApJS*, 198, 2
 Laine, S., van der Marel, R. P., Lauer, T. R., et al. 2004, in *Coevolution of Black Holes and Galaxies*, ed. L. C. Ho, 36
 Law, D. R., Yan, R., Bershady, M. A., et al. 2015, *AJ*, 150, 19

- Lee, J. H., Lee, M. G., Mun, J. Y., Cho, B. S., & Kang, J. 2022, *ApJ*, 931, L22
- Lewis, I., Balogh, M., De Propriis, R., et al. 2002, *MNRAS*, 334, 673
- Lin, L., Hsieh, B.-C., Pan, H.-A., et al. 2019, *ApJ*, 872, 50
- Lin, X., Wang, J., Kilborn, V., et al. 2023, *ApJ*, 956, 148
- Loni, A., Serra, P., Sarzi, M., et al. 2023, *MNRAS*, 523, 1140
- Lotz, J. M., Jonsson, P., Cox, T. J., et al. 2011, *ApJ*, 742, 103
- Lotz, J. M., Primack, J., & Madau, P. 2004, *AJ*, 128, 163
- Mahoro, A., Pović, M., Nkundabakura, P., Nyiransengiyumva, B., & Väisänen, P. 2019, *MNRAS*, 485, 452
- Mao, Z., Kodama, T., Pérez-Martínez, J. M., et al. 2022, *A&A*, 666, A141
- Mishra, P. K., Wadadekar, Y., & Barway, S. 2018, *MNRAS*, 478, 351
- Mowla, L., van der Wel, A., van Dokkum, P., & Miller, T. B. 2019, *ApJ*, 872, L13
- Nevin, R., Blecha, L., Comerford, J., et al. 2023, *MNRAS*, 522, 1
- Oser, L., Ostriker, J. P., Naab, T., Johansson, P. H., & Burkert, A. 2010, *ApJ*, 725, 2312
- Pak, M., Lee, J. H., Jeong, H., et al. 2019, *ApJ*, 880, 149
- Pérez-Millán, D., Fritz, J., González-Lópezlira, R. A., et al. 2023, *MNRAS*, 521, 1292
- Querejeta, M., Eliche-Moral, M. C., Tapia, T., et al. 2015, *A&A*, 579, L2
- Rathore, H., Kumar, K., Mishra, P. K., Wadadekar, Y., & Bait, O. 2022, *MNRAS*, 513, 389
- Salim, S. 2014, *Serbian Astronomical Journal*, 189, 1
- Salim, S., Boquien, M., & Lee, J. C. 2018, *ApJ*, 859, 11
- Salim, S., Lee, J. C., Janowiecki, S., et al. 2016, *ApJS*, 227, 2
- Salpeter, E. E. 1955, *ApJ*, 121, 161
- Sánchez, S. F. 2020, *ARA&A*, 58, 99
- Sánchez, S. F., Pérez, E., Sánchez-Blázquez, P., et al. 2016a, *Rev. Mexicana Astron. Astrofis.*, 52, 171
- Sánchez, S. F., Pérez, E., Sánchez-Blázquez, P., et al. 2016b, *Rev. Mexicana Astron. Astrofis.*, 52, 21
- Schawinski, K., Lintott, C., Thomas, D., et al. 2009, *MNRAS*, 396, 818
- Schawinski, K., Thomas, D., Sarzi, M., et al. 2007, *MNRAS*, 382, 1415
- Shields, G. A., Skillman, E. D., & Kennicutt, Robert C., J. 1991, *ApJ*, 371, 82
- Smirnova-Pinchukova, L., Husemann, B., Davis, T. A., et al. 2022, *A&A*, 659, A125
- Strateva, I., Ivezić, Ž., Knapp, G. R., et al. 2001, *AJ*, 122, 1861
- Tabor, M., Merrifield, M., Aragón-Salamanca, A., et al. 2017, *MNRAS*, 466, 2024
- Taylor, M. B. 2005, in *Astronomical Society of the Pacific Conference Series*, Vol. 347, *Astronomical Data Analysis Software and Systems XIV*, ed. P. Shopbell, M. Britton, & R. Ebert, 29
- Tous, J. L., Domínguez-Sánchez, H., Solanes, J. M., & Perea, J. D. 2023, *ApJ*, 942, 48
- Tremonti, C. A., Heckman, T. M., Kauffmann, G., et al. 2004, *ApJ*, 613, 898
- Vaughan, S. P., Barone, T. M., Croom, S. M., et al. 2022, *MNRAS*, 516, 2971
- Vázquez-Mata, J. A., Hernández-Toledo, H. M., Avila-Reese, V., et al. 2022, *MNRAS*, 512, 2222
- Vollmer, B. 2013, in *Planets, Stars and Stellar Systems. Volume 6: Extragalactic Astronomy and Cosmology*, ed. T. D. Oswalt & W. C. Keel, Vol. 6, 207
- Wang, D., Croom, S. M., Bryant, J. J., et al. 2022, *MNRAS*, 516, 3411
- Wang, E., Lilly, S. J., Pezzulli, G., & Matthee, J. 2019, *ApJ*, 877, 132
- Wang, H., Mo, H. J., Yang, X., et al. 2016, *ApJ*, 831, 164
- Xiao, M.-Y., Gu, Q.-S., Chen, Y.-M., & Zhou, L. 2016, *ApJ*, 831, 63
- Xu, K., Gu, Q., Lu, S., et al. 2022, *MNRAS*, 509, 1237
- Yan, R., Bundy, K., Law, D. R., et al. 2016, *AJ*, 152, 197
- Yun, K., Pillepich, A., Zinger, E., et al. 2019, *MNRAS*, 483, 1042
- Zhou, S., Li, C., Hao, C.-N., et al. 2021, *ApJ*, 916, 38

Appendix A: Detailed information on our two samples

Table A.1: Detailed Information of SFS0s_HE

PLATE_IFU (1)	Redshift (2)	R.A. (deg) (3)	Decl. (deg) (4)	$\log(M_*/M_\odot)$ (5)	$\log(\text{SFR}_{\text{SED}} (M_\odot\text{yr}^{-1}))$ (6)	Sérsic index (7)	$\eta_{a,k}$ (8)	$R_e(r)$ (9)	B/T (10)	T_Type (11)	P_LTG (12)	P_S0 (13)	$\text{EW}_{H\alpha}$ (Å) (14)
10505-6104	0.0217	140.7277	33.1420	9.336 ± 0.032	-1.135 ± 0.130	0.21 ± 0.03	0.93	3.28	0.46	-2.288 ± 0.570	0.48	0.79	-25.86 ± 6.42
11759-3703	0.0201	146.8423	0.7408	9.275 ± 0.058	-0.506 ± 0.102	2.15 ± 0.58	2.38	3.93	0.27	-1.143 ± 0.661	0.02	0.57	-31.06 ± 2.37
11761-6104	0.0276	195.9200	53.7232	10.439 ± 0.021	-1.979 ± 0.704	8.00 ± 0.48	1.73	6.39	0.43	-1.303 ± 0.505	0.05	0.71	-10.48 ± 1.18
11834-1902	0.0435	223.0809	-0.2692	10.197 ± 0.027	-0.162 ± 0.093	1.04 ± 0.04	0.20	2.11	0.49	-1.588 ± 0.724	0.04	0.59	-21.30 ± 1.47
12079-3704	0.0431	30.4308	-1.0698	11.064 ± 0.016	0.208 ± 0.158	1.96 ± 0.08	1.70	5.05	0.54	-0.441 ± 0.790	0.04	0.54	-7.16 ± 0.99
7975-6104	0.0788	324.8916	10.4835	11.238 ± 0.034	0.650 ± 0.121	2.01 ± 0.06	0.83	4.04	0.67	-0.452 ± 0.710	0.17	0.58	-11.81 ± 2.57
8082-6101	0.0213	50.1452	-1.0959	9.061 ± 0.070	-0.402 ± 0.121	0.99 ± 0.06	2.59	5.55	0.29	-0.381 ± 0.601	0.08	0.53	-8.02 ± 1.95
8083-3702	0.0238	49.9732	0.3914	9.719 ± 0.042	-0.449 ± 0.133	1.15 ± 0.05	1.10	3.01	0.64	-0.106 ± 0.630	0.24	0.60	-22.02 ± 2.39
8097-3704	0.0258	27.2633	12.8736	9.552 ± 0.041	-0.596 ± 0.126	1.51 ± 0.44	0.61	2.53	0.68	-0.953 ± 0.610	0.09	0.71	-31.33 ± 4.12
8149-3703	0.0267	119.3568	27.4403	9.765 ± 0.036	-1.358 ± 0.427	4.14 ± 0.24	0.94	3.04	0.62	-0.258 ± 0.600	0.02	0.56	-7.59 ± 0.99
8249-3703	0.0264	139.7204	45.7278	9.873 ± 0.018	0.153 ± 0.023	1.00 ± 0.02	1.07	4.56	0.20	-2.339 ± 0.459	0.02	0.57	-69.59 ± 9.29
8262-3702	0.0242	183.6598	43.5362	10.264 ± 0.038	0.205 ± 0.061	1.06 ± 0.02	1.43	4.84	0.28	-0.122 ± 0.400	0.09	0.56	-17.31 ± 3.53
8336-3701	0.0179	210.3769	38.5159	9.157 ± 0.037	-1.018 ± 0.075	6.29 ± 0.82	1.58	4.64	0.59	-1.058 ± 0.564	0.45	0.80	-18.15 ± 2.54
8588-1901	0.0364	249.7171	40.1993	9.924 ± 0.060	-0.304 ± 0.186	0.19 ± 0.02	0.31	1.77	0.24	-1.150 ± 0.628	0.20	0.90	-31.81 ± 3.32
8622-3704	0.0402	351.2176	14.1389	10.075 ± 0.064	-0.005 ± 0.016	5.58 ± 0.76	0.76	2.83	0.68	-0.228 ± 0.499	0.04	0.53	-29.97 ± 3.13
8715-6101	0.0543	119.1058	51.3446	10.789 ± 0.037	0.131 ± 0.080	2.21 ± 0.13	1.23	3.19	0.37	-2.069 ± 0.630	0.03	0.61	-6.93 ± 0.36
8985-3702	0.0238	204.0827	32.8751	9.655 ± 0.036	-0.445 ± 0.076	2.02 ± 0.08	0.57	4.73	0.29	-0.921 ± 0.760	0.09	0.54	-9.01 ± 1.29
9029-6103	0.0304	246.7944	42.6789	10.099 ± 0.030	-0.538 ± 0.158	6.66 ± 0.63	1.46	5.61	0.10	-3.359 ± 0.563	0.43	0.73	-7.21 ± 0.36
9037-3702	0.0188	234.8425	43.8654	9.741 ± 0.036	-0.44 ± 0.125	5.73 ± 0.39	0.57	4.46	0.76	-2.220 ± 0.521	0.02	0.58	-18.75 ± 2.45
9491-3701	0.0415	119.1066	17.9741	9.807 ± 0.038	-0.128 ± 0.083	1.70 ± 0.09	1.74	2.61	0.52	-2.421 ± 0.699	0.08	0.92	-17.92 ± 2.07
9499-1901	0.0454	119.3980	25.8073	10.361 ± 0.030	-0.319 ± 0.220	1.80 ± 0.09	1.36	1.42	0.60	-2.219 ± 0.625	0.04	0.51	-9.16 ± 0.32
9873-12702	0.0252	194.5855	27.4294	9.304 ± 0.041	-0.769 ± 0.080	0.84 ± 0.03	2.37	3.54	0.30	-2.230 ± 0.522	0.12	0.92	-14.14 ± 1.39
9875-3704	0.0196	195.1152	27.6252	9.371 ± 0.047	-1.936 ± 0.958	1.98 ± 0.06	2.22	3.34	0.75	-2.340 ± 0.450	0.01	0.51	-71.61 ± 5.56

Notes: The columns show (1) the MaNGA_ID PLATE_IFU of our targets; (2) Redshift; (3) R.A. (deg); (4) Decl. (deg); (5), (6) the stellar mass and SFR from [Salim et al. \(2016, 2018\)](#); (7) Sérsic index; (8) the projected number density parameter of the galaxy from GEMA_VAC; (9) R_e ; (10) bulge-to-total light ratio; (11) T_Type ; (12) probability of LTG; (13) probability of S0; (14) the $H\alpha$ equivalent width within the center of 2.5". Pipe3D catalog defaults equivalent width to negative for emission lines ([Sánchez 2020](#)).

Table A.2: Detailed Information of SFS0s_HE

PLATE_IFU (1)	Redshift (2)	R.A. (deg) (3)	Decl. (deg) (4)	$\log(M_*/M_\odot)$ (5)	$\log(\text{SFR}_{\text{SED}} (M_\odot \text{yr}^{-1}))$ (6)	Sérsic index (7)	η_k (8)	$R_e(r)$ (9)	B/T (10)	T_Type (11)	P_LTG (12)	P_S0 (13)	EW_H α (Å) (14)
10218-1901	0.0222	118.0347	17.9303	9.423 ± 0.037	-0.163 ± 0.029	0.62 ± 0.01	-999	1.90	0.55	-0.635 ± 0.521	0.04	0.52	-85.24 ± 16.16
10497-1901	0.0406	120.6247	17.2847	9.864 ± 0.025	-0.486 ± 0.114	1.63 ± 0.11	-999	1.71	0.74	-1.198 ± 0.370	0.29	0.86	-13.68 ± 0.73
10841-3704	0.0227	142.3593	2.0707	9.580 ± 0.036	-0.833 ± 0.189	1.71 ± 0.38	-999	2.94	0.29	-0.450 ± 0.340	0.13	0.59	-6.14 ± 0.55
11010-6101	0.0233	198.2229	23.6346	9.536 ± 0.047	-0.495 ± 0.078	0.20 ± 0.01	-999	5.62	0.26	-4.258 ± 0.618	0.10	0.97	-13.99 ± 1.72
11753-3701	0.0933	146.6613	2.6589	11.452 ± 0.031	0.943 ± 0.064	6.32 ± 1.00	-999	2.77	0.58	-1.580 ± 0.474	0.02	0.60	-14.49 ± 0.76
11759-3701	0.0457	145.5940	0.3094	10.505 ± 0.053	0.156 ± 0.202	2.89 ± 0.32	-999	2.68	0.44	-0.740 ± 0.592	0.15	0.75	-27.53 ± 7.32
11823-1901	0.0368	248.2540	27.5934	9.41 ± 0.055	-0.275 ± 0.059	1.10 ± 0.03	-999	1.88	0.56	-1.468 ± 0.584	0.39	0.91	-51.74 ± 10.46
11826-3702	0.0363	189.4614	38.8770	9.522 ± 0.043	-0.511 ± 0.070	3.61 ± 0.39	-999	2.37	0.70	-1.761 ± 0.563	0.37	0.79	-36.93 ± 7.54
11838-1902	0.0346	156.7275	-0.5415	11.321 ± 0.053	0.697 ± 0.114	0.67 ± 0.02	-999	3.39	0.33	-1.011 ± 0.714	0.01	0.46	-16.94 ± 0.82
11948-1901	0.0364	250.2385	32.2889	9.605 ± 0.058	0.207 ± 0.087	2.72 ± 0.18	-999	1.69	0.52	-0.117 ± 0.655	0.02	0.61	-81.29 ± 5.05
11952-12703	0.0338	254.4507	27.4168	10.413 ± 0.03	0.022 ± 0.001	0.89 ± 0.02	-999	10.64	0.31	-1.635 ± 0.783	0.12	0.67	-10.40 ± 1.20
11975-1902	0.0358	252.8002	25.6509	9.512 ± 0.037	-0.385 ± 0.035	2.23 ± 0.39	-999	2.20	0.45	-1.635 ± 0.783	0.45	0.87	-39.95 ± 3.85
12085-3701	0.0358	346.4024	13.6225	9.960 ± 0.051	-0.258 ± 0.012	5.57 ± 2.04	-999	2.13	0.66	-0.588 ± 0.581	0.05	0.67	-19.03 ± 1.73
12089-1902	0.0171	352.3083	15.4361	9.328 ± 0.026	-0.718 ± 0.018	0.94 ± 0.05	-999	3.56	0.19	-3.627 ± 0.600	0.15	0.95	-19.80 ± 1.71
12483-1901	0.0223	185.9798	33.9287	9.259 ± 0.044	-0.685 ± 0.093	2.38 ± 0.21	-999	1.90	0.54	-0.934 ± 0.483	0.18	0.58	-22.94 ± 1.98
8138-3704	0.0263	118.0205	44.1615	9.995 ± 0.027	-0.310 ± 0.091	0.88 ± 0.03	-999	2.21	0.46	-1.747 ± 0.558	0.02	0.43	-18.07 ± 0.99
8140-1902	0.0407	117.7660	41.9735	9.926 ± 0.043	0.023 ± 0.002	0.55 ± 0.05	-999	1.79	0.38	-0.657 ± 0.434	0.36	0.78	-52.20 ± 2.55
8155-1902	0.0234	53.7267	-0.7889	9.479 ± 0.063	-0.431 ± 0.062	0.90 ± 0.06	-999	2.79	0.41	-1.211 ± 0.512	0.08	0.52	-40.74 ± 3.28
8158-1901	0.0384	60.8593	-5.4918	9.450 ± 0.061	-0.148 ± 0.063	1.00 ± 0.08	-999	1.93	0.57	-1.810 ± 0.556	0.30	0.84	-46.96 ± 3.73
8241-1902	0.0383	125.2728	17.8198	9.653 ± 0.064	-0.181 ± 0.058	0.93 ± 0.03	-999	2.23	0.51	-1.049 ± 0.646	0.12	0.78	-50.47 ± 5.33
8243-3701	0.0431	128.1644	53.2332	10.366 ± 0.014	-1.993 ± 0.561	7.00 ± 0.43	-999	2.73	0.73	-1.516 ± 0.597	0.02	0.45	-89.66 ± 15.12
8259-1902	0.0242	177.7961	44.0088	9.854 ± 0.031	-0.407 ± 0.100	0.88 ± 0.01	-999	2.86	0.33	-1.879 ± 0.434	0.16	0.88	-17.37 ± 2.17
8261-1901	0.0231	182.8574	44.4360	9.589 ± 0.043	-0.332 ± 0.073	0.36 ± 0.01	-999	2.36	0.59	-0.484 ± 0.577	0.02	0.59	-40.90 ± 2.30
8313-6103	0.0238	239.4366	41.7095	9.906 ± 0.041	0.052 ± 0.058	1.25 ± 0.02	-999	3.37	0.33	-0.938 ± 0.572	0.03	0.58	-24.91 ± 6.06
8314-3702	0.0302	240.8477	39.9857	10.267 ± 0.029	0.110 ± 0.078	6.29 ± 0.83	-999	4.08	0.59	-0.822 ± 0.651	0.03	0.49	-19.99 ± 2.81
8315-9101	0.0626	235.7861	40.0486	11.105 ± 0.04	0.321 ± 0.207	1.61 ± 0.68	-999	4.19	0.32	-0.813 ± 0.502	0.31	0.78	-8.88 ± 0.58
8323-3701	0.0332	195.3896	34.1167	9.616 ± 0.032	-0.696 ± 0.148	0.98 ± 0.01	-999	2.62	0.45	-0.842 ± 0.503	0.10	0.75	-12.74 ± 1.78
8323-3703	0.0675	196.4398	34.6811	11.210 ± 0.027	0.557 ± 0.099	1.78 ± 0.16	-999	3.01	0.49	-0.227 ± 0.649	0.05	0.54	-7.13 ± 0.88
8448-6101	0.0355	165.9620	23.0065	9.431 ± 0.045	-0.497 ± 0.048	0.67 ± 0.02	-999	3.35	0.46	-1.021 ± 0.688	0.02	0.54	-33.99 ± 6.95
8455-1902	0.0262	155.7087	39.3689	9.626 ± 0.033	-0.429 ± 0.093	0.68 ± 0.04	-999	2.15	0.48	-1.397 ± 0.437	0.21	0.90	-41.25 ± 2.81
8459-1902	0.0170	148.5025	43.0448	9.031 ± 0.042	-1.022 ± 0.057	1.19 ± 0.02	-999	3.11	0.38	-2.240 ± 0.734	0.38	0.82	-52.54 ± 11.93
8462-3704	0.0398	143.3743	37.5026	9.986 ± 0.024	-0.380 ± 0.068	0.28 ± 0.01	-999	2.29	0.56	-1.127 ± 0.471	0.19	0.87	-15.41 ± 2.60
8568-3703	0.0226	155.6931	37.6735	9.462 ± 0.074	0.034 ± 0.006	5.67 ± 0.62	-999	4.40	0.45	-1.043 ± 0.508	0.10	0.55	-115.91 ± 29.09
8652-1902	0.0460	331.0860	-0.5028	10.289 ± 0.026	-0.027 ± 0.094	1.53 ± 0.02	-999	2.17	0.84	-0.448 ± 0.477	0.12	0.80	-15.70 ± 2.39
8939-3701	0.0198	125.3617	24.4531	10.136 ± 0.034	-0.139 ± 0.125	1.07 ± 0.01	-999	5.26	0.38	-0.603 ± 0.714	0.03	0.53	-25.57 ± 4.92
8940-6102	0.0276	120.8669	25.1027	10.540 ± 0.042	-0.156 ± 0.012	1.49 ± 0.17	-999	2.65	0.02	-0.639 ± 0.657	0.07	0.58	-45.34 ± 5.12
8983-6102	0.0313	205.1829	25.9084	10.355 ± 0.029	-0.190 ± 0.142	0.17 ± 0.03	-999	7.13	0.37	-1.370 ± 0.803	0.44	0.78	-31.05 ± 3.66
9035-12702	0.0383	236.5584	44.9646	9.964 ± 0.033	-0.208 ± 0.098	8.00 ± 0.89	-999	2.22	0.52	-1.568 ± 0.700	0.45	0.87	-24.93 ± 2.10
9040-3703	0.0384	244.8737	28.5169	9.688 ± 0.061	-0.236 ± 0.089	2.05 ± 0.23	-999	2.57	0.09	-0.556 ± 0.700	0.06	0.59	-38.84 ± 4.14
9092-1901	0.0344	240.6321	24.7622	9.488 ± 0.045	-0.444 ± 0.081	2.71 ± 0.70	-999	1.39	0.17	-0.029 ± 0.489	0.17	0.74	-23.85 ± 2.41
9181-1902	0.0399	120.8730	38.4423	9.930 ± 0.024	-0.448 ± 0.132	0.90 ± 0.06	-999	1.85	0.83	-0.550 ± 0.437	0.15	0.80	-22.10 ± 2.15
9183-6101	0.0225	122.0845	39.0236	10.267 ± 0.031	-0.028 ± 0.119	0.50 ± 0.03	-999	3.25	0.80	-0.240 ± 0.614	0.37	0.69	-28.62 ± 1.31
9185-9101	0.0563	256.2123	34.8173	10.611 ± 0.063	1.488 ± 0.053	1.93 ± 0.17	-999	7.32	0.39	-0.367 ± 0.652	0.15	0.58	-96.38 ± 9.18
9187-3704	0.0374	312.1987	-6.5032	9.596 ± 0.043	-0.339 ± 0.052	0.64 ± 0.03	-999	2.34	0.32	-0.033 ± 0.485	0.10	0.52	-54.62 ± 4.44
9488-1902	0.0182	127.0117	20.9967	9.072 ± 0.023	-0.741 ± 0.012	1.55 ± 0.03	-999	2.95	0.32	-1.123 ± 0.620	0.14	0.52	-36.61 ± 3.96
9863-3703	0.0274	194.5132	26.9160	10.515 ± 0.02	-1.603 ± 0.600	1.11 ± 0.06	-999	4.05	0.34	-0.267 ± 0.568	0.05	0.76	-8.48 ± 2.70
9865-1901	0.0134	222.4368	50.7109	9.592 ± 0.027	-0.420 ± 0.148	1.10 ± 0.03	-999	3.57	0.13	-0.918 ± 0.703	0.09	0.86	-24.78 ± 3.74
9872-3701	0.0197	233.2320	42.4383	10.083 ± 0.043	0.012 ± 0.057	0.63 ± 0.01	-999	3.84	0.33	-0.418 ± 0.644	0.15	0.82	-32.23 ± 5.75

Notes: All columns are the same as in Table A.1.